

$B \rightarrow K$ and $D \rightarrow K$ form factors from fully relativistic lattice QCDW. G. Parrott^{*,} C. Bouchard^{†,} and C. T. H. Davies^{‡,}(HPQCD collaboration)[§]*SUPA, School of Physics and Astronomy, University of Glasgow, Glasgow G12 8QQ, United Kingdom* (Received 3 August 2022; revised 15 November 2022; accepted 18 November 2022; published 24 January 2023)

We present the result of lattice QCD calculation of the scalar, vector and tensor form factors for the $B \rightarrow K\ell^+\ell^-$ decay, across the full physical range of momentum transfer. We use the highly improved staggered quark (HISQ) formalism for all valence quarks on eight ensembles of gluon-field configurations generated by the MILC collaboration. These include four flavors of HISQ quarks in the sea, with three ensembles having the light u/d quarks at physical masses. In the first fully relativistic calculation of these form factors, we use the heavy-HISQ method. This allows us to determine the form factors as a function of heavy-quark mass from the c to the b , and so we also obtain new results for the $D \rightarrow K$ tensor form factor. The advantage of the relativistic formalism is that we can match the lattice weak currents to their continuum counterparts much more accurately than in previous calculations; our scalar and vector currents are renormalized fully nonperturbatively and we use a well-matched intermediate momentum-subtraction scheme for our tensor current. Our scalar and vector $B \rightarrow K$ form factors have uncertainties of less than 4% across the entire physical q^2 range and the uncertainty in our tensor form factor is less than 7%. Our heavy-HISQ method allows us to map out the dependence on heavy-quark mass of the form factors and we can also see the impact of changing spectator quark mass by comparing to earlier HPQCD results for the same quark weak transition but for heavier mesons.

DOI: [10.1103/PhysRevD.107.014510](https://doi.org/10.1103/PhysRevD.107.014510)**I. INTRODUCTION**

Here we study the $B \rightarrow K\ell\bar{\ell}$ decay, where ℓ can be a charged lepton or a neutrino. The decay involves the $b \rightarrow s$ flavor-changing neutral current (FCNC) and is highly suppressed in the Standard Model (SM) since it must proceed through loop diagrams with at least one off-diagonal (and hence small) element of the Cabbibo-Kobayashi-Maskawa (CKM) matrix [1,2]. This means that the process is highly sensitive to the existence of “new” particles which may appear in the loops.

The increasing quantity of experimental data being collected [3–15] allows for much stronger bounds to be placed on rare decays such as this one, which often rely on huge numbers of collisions to be observed to register just a

handful of events. In order to take advantage of this improved precision in our search for new physics beyond the SM [16–23], we must meet these results with improved theoretical uncertainty. At present, lattice quantum chromodynamics (QCD) is the only model-independent method for calculating hadronic form factors for such decays. The form factors can be used to construct the dominant contribution to the differential branching fraction, for comparison to experiment, in regions of q^2 away from $c\bar{c}$ and $u\bar{u}$ resonances.

Previous full-lattice QCD calculations used gluon-field configurations generated by the MILC collaboration that include the effect of 3 flavors of sea quarks in the asqtad formalism [24]. Reference [25] used the nonrelativistic (NRQCD) [26] formalism for the b quarks and highly improved staggered quarks (HISQ) [27] for other valence flavors. Similarly, [28] used Fermilab b quarks [29] and the asqtad formalism for other flavors. Both of these calculations used $\mathcal{O}(\alpha_s)$ perturbation theory to match the lattice weak current operators to their continuum counterparts. Missing higher-order effects in the matching are then a significant source of uncertainty in the form factors. In addition the calculations were done at relatively low values of the K meson spatial momentum in the B meson rest frame (i.e. close to zero recoil).

*w.parrott.1@research.gla.ac.uk

†chris.bouchard@glasgow.ac.uk

‡christine.davies@glasgow.ac.uk

§<http://www.physics.gla.ac.uk/HPQCD>.

Published by the American Physical Society under the terms of the Creative Commons Attribution 4.0 International license. Further distribution of this work must maintain attribution to the author(s) and the published article's title, journal citation, and DOI. Funded by SCOAP³.

In this paper we present the first fully relativistic calculation, using HISQ formalism for all valence quarks and working on MILC $N_f = 2 + 1 + 1$ gluon-field ensembles that include HISQ quarks in the sea [30,31]. The calculation mirrors the heavy-HISQ approach used successfully in several other recent HPQCD calculations (e.g. [32–35]). By using a relativistic treatment we eliminate the matching errors arising from effective theory treatment of the b quark in previous methods. We are also able to cover the full physical q^2 range of the decay process directly.

Our method involves calculating the form factors for a range of heavy-quark masses from that of the c quark up to that of the b . We thus obtain results for form factors for both $D \rightarrow K$ decay and for $B \rightarrow K$ decay and the functional form in heavy-quark mass that connects them. The vector and scalar $D \rightarrow K$ form factors were recently used in an analysis of the $D \rightarrow K\ell\bar{\nu}$ weak semileptonic decay process and, combined with experimental results, gave a 1%-accurate determination of the CKM element V_{cs} [36]. That analysis showed very good agreement between the q^2 dependence of the vector form factor calculated in lattice QCD and that inferred from the experimental results for the differential decay rate. This provides a very solid test that our lattice QCD form factors at the c quark mass end of our heavy-quark mass range describe experimental results for a case ($D \rightarrow K\ell\bar{\nu}$) where no new physics is expected. Here we give the tensor form factor for $D \rightarrow K$ decay, not calculated in [36].

In this work we will focus on the calculation of the form factors themselves, while an accompanying article [37] will study the phenomenological implications from our results. Section II sets out the calculational framework and then Sec. III describes the fits and data analysis. Section IV shows the results as a function of q^2 , detailing the changes between $D \rightarrow K$ and $B \rightarrow K$, as well as comparing $B \rightarrow K$ form factors with those for $B_c \rightarrow D_s$ [38], which differ in spectator quark mass. We also provide complete error budgets for the form factors and compare to expectations from heavy quark effective theory. Section V gives our conclusions.

II. LATTICE CALCULATION

A. Form factors

The quantities of interest here are the scalar, vector and tensor form factors $f_0(q^2)$, $f_+(q^2)$, and $f_T(q^2)$, which are functions of $q^2 = (p_B - p_K)^2$. We can construct these form factors from hadronic matrix elements between the B and K which we calculate on the lattice.

Our heavy-HISQ approach works by determining a set of matrix elements for mesons in which the b quark is replaced by a heavy quark with mass $m_h < m_b$. The heaviest mass on the finest ensemble we use is close to the b mass ($m_h/m_b \approx 0.85$). We denote the resulting pseudoscalar heavy-light mesons generically by H .

We compute these matrix elements for a variety of masses ranging from that of the charm quark upwards, across the range $0 \leq q^2 \leq q_{\max}^2 = (M_H - M_K)^2$, which is the full physical range of q^2 for the decay of a heavy-light meson of mass M_H . As $m_h \rightarrow m_b$ this becomes the full range for the $B \rightarrow K$ decay.

The connection between the matrix elements of the lattice scalar, vector and tensor currents and the form factors is

$$Z_V \langle K | V_{\text{latt}}^\mu | \hat{H} \rangle = f_+(q^2) \left(p_H^\mu + p_K^\mu - \frac{M_H^2 - M_K^2}{q^2} q^\mu \right) + f_0(q^2) \frac{M_H^2 - M_K^2}{q^2} q^\mu, \quad (1)$$

$$\langle K | S_{\text{latt}} | H \rangle = \frac{M_H^2 - M_K^2}{m_h - m_s} f_0(q^2), \quad (2)$$

$$Z_T(\mu) \langle \hat{K} | T_{\text{latt}}^{k0} | \hat{H} \rangle = \frac{2iM_H p_K^k}{M_H + M_K} f_T(q^2, \mu). \quad (3)$$

Here q^μ is the 4-momentum transfer and q^2 its square. We work in the rest frame of the H such that $p_H^0 = M_H$. The K meson is given spatial momentum \vec{p}_K in the (1, 1, 1) direction, making all spatial directions equivalent, and we take spatial component $k = 1$ for the tensor form factor. Z_V and Z_T are renormalization factors for the lattice vector and tensor currents that we discuss below. Note that the tensor form factor has a renormalization scale μ associated with it. m_h and m_s in Eq. (2) are the lattice valence quark masses for the h and s quarks.

Requiring that the matrix elements are finite as $q^2 \rightarrow 0$ gives the constraint

$$f_+(0) = f_0(0). \quad (4)$$

We will make use of this condition later.

Bilinears constructed from staggered quarks have a ‘‘taste’’ degree of freedom, ξ , and we need to arrange the tastes of mesons and lattice currents appropriately so that tastes cancel in the correlation functions that we calculate. Here we follow the approach used in [36], where the rationale is described in more detail. We aim to have local operators for all of the currents (with ψ and $\bar{\psi}$ at the same point) because these are least noisy and have no tree-level discretization errors. This means that we must use point-split operators for the meson creation and annihilation operators in some cases. In spin-taste notation [27], the lattice scalar, vector and tensor currents are $S = \bar{\psi}_s 1 \otimes 1 \psi_h$, $V^\mu = \bar{\psi}_s \gamma^\mu \otimes \xi^\mu \psi_h$ and $T^{k0} = \bar{\psi}_s \gamma^k \gamma^0 \otimes \xi^k \xi^0 \psi_h$. $H = \bar{\psi}_l \gamma^5 \otimes \xi^5 \psi_h$ and $\hat{H} = \bar{\psi}_l \gamma^5 \gamma^0 \otimes \xi^5 \xi^0 \psi_h$ denote Goldstone and local non-Goldstone heavy-light pseudoscalar mesons, respectively. Similarly for the kaons, $K = \bar{\psi}_s \gamma^5 \otimes \xi^5 \psi_l$

and $\hat{K} = \bar{\psi}_s \gamma^5 \otimes \xi^5 \xi^1 \psi_l$ denote Goldstone and point-split non-Goldstone strange-light pseudoscalar mesons, respectively.

We use the local temporal component of the vector current, V^0 , for most results but we also include some additional spatial current data with the local vector current V^k in the $k = 1$ direction. The reason for this is that the vector form factor determined from the temporal vector current has a numerical problem at large q^2 from the way that it is constructed [34]. Rearranging Eq. (1) we have

$$f_+(q^2) = \frac{1}{A^\mu - B^\mu} (Z_V \langle K | V^\mu | \hat{H} \rangle - f_0(q^2) B^\mu), \quad (5)$$

where $A^\mu = p_H^\mu + p_K^\mu$ and $B^\mu = \frac{M_H^2 - M_K^2}{q^2} q^\mu$. Both numerator and denominator vanish as $q^2 \rightarrow q_{\max}^2$ amplifying the uncertainties and leading to large statistical errors in f_+ at large q^2 . One solution to this issue is to use a spatial component of the vector current, with spin taste $\gamma^1 \otimes \xi^1$. This component requires a point-split $\gamma^5 \otimes \xi^5 \xi^1$ kaon (\hat{K}), which we have already used in the tensor case, and the Goldstone heavy-light pseudoscalar (H). At low q^2 the point-split kaon makes this component noisier than the temporal case which we predominantly use, but at large q^2 the resulting f_+ does not suffer from the same dramatic growth in uncertainties and so is to be preferred. We include in our dataset a handful of V^1 matrix elements, at large q^2 and mass, on our two finest ensembles to supplement our comprehensive V^0 data. We use the same Z_V for both V^0 and V^1 since any difference between the two cases for our relativistic action is purely a discretization effect. We will denote the form factors obtained in the two cases $f_+^{V^0}$ and $f_+^{V^1}$ where the distinction is relevant. We discuss a comparison of the two cases in Sec. III.

B. Current normalization

The fact that the partially conserved vector current (PCVC) relation holds for the HISQ action means that the scalar form factor $f_0(q^2)$ can be obtained from the matrix element of the local scalar current using Eq. (2) with absolute normalization [39]. We would also need no renormalization for the vector current if we used the conserved current [40]. Here, however, we use the much simpler local vector current and this requires renormalization. The renormalization factor, Z_V , can be calculated fully nonperturbatively using the PCVC relation [39,41]. We apply it in the temporal vector case at zero recoil, where both the H and K mesons are at rest and it gives the most accurate results [34],

$$Z_V = \frac{(m_h - m_s) \langle K | S | H \rangle}{(M_H - M_K) \langle K | V^0 | \hat{H} \rangle} \Big|_{q^2=q_{\max}^2}. \quad (6)$$

We also calculate the tensor form factor and the tensor current requires renormalization. Z_T in Eq. (3) takes the lattice local tensor current to that in the $\overline{\text{MS}}$ scheme at a specific renormalization scale μ . Z_T can be determined accurately for the HISQ action [42] using an intermediate momentum-subtraction scheme, called RI-SMOM, that can be matched through $\mathcal{O}(\alpha_s^3)$ to $\overline{\text{MS}}$ [43]. This makes the renormalization factor much more accurate than the $\mathcal{O}(\alpha_s)$ renormalization factors used in previous calculations of the $B \rightarrow K$ tensor form factor [25,28]. Note that the intermediate momentum-subtraction scheme is implemented nonperturbatively on the lattice and so attention must be paid to nonperturbative artifacts (“condensates”) that can appear as inverse powers of the intermediate renormalization scale. These are analyzed using fits to multiple intermediate scales in [42]. We use corrected Z_T values from Table VIII of [42] in which these artifacts have been removed. We will give final results for f_T for $B \rightarrow K$ at a scale $\mu = 4.8$ GeV appropriate to m_b (taken as the approximate value of the b quark pole mass); for $D \rightarrow K$ we will give values at a lower scale ($\mu = 2$ GeV). f_T values can be run between scales straightforwardly [42].

C. Simulation details

The calculation was run on MILC gluon-field ensembles [30,31] that include in the sea two degenerate light quarks, strange and charm quarks, with masses $m_l^{\text{sea}}, m_s^{\text{sea}}, m_c^{\text{sea}}$, using the HISQ action [27]. The eight ensembles used have parameters listed in Table I. Sets 1, 2 and 3 have physical light-quark masses, whilst sets 4–8 have $m_l^{\text{sea/val}} = 0.2m_s^{\text{sea}}$. Note that the valence light-quark masses are the same as those in the sea; the valence strange-quark masses are tuned more accurately than the sea strange-quark masses and so differ slightly from them. The valence strange-quark masses are tuned [44] to give the physical value for the mass of the $s\bar{s}$ pseudoscalar meson known as the η_s (which does not appear in the real world), whose mass is determined in terms of the pion and kaon masses in [45]. The gluon action is Symanzik improved to remove discretization errors through $\mathcal{O}(\alpha_s a^2)$ [46].

A significant portion of the data used here overlaps with those used for $D \rightarrow K$ form factors in [36]. Sets 1 and 2 are identical, while other sets share the lowest mass (the charm), but include additional masses and the extra tensor current insertion. This means that, while the calculation produced a slightly different set of $D \rightarrow K$ scalar and vector form factors, these are correlated to those in [36] and as such should not be viewed as an independent calculation. The $D \rightarrow K$ tensor form factor, however, was not calculated in [36] and will be presented here. The valence heavy-quark masses used on each ensemble are given in Table II.

In order to compute the matrix elements needed for our form factors, we must extract the amplitudes from three-point correlation functions built on the lattice. A schematic

TABLE I. Gluon-field ensembles used in this work, numbered in column 1, with gauge coupling values, β , in column 2. The Wilson flow parameter [47] is used to calculate the lattice spacing a via values for w_0/a [35] in column 3. We use $w_0 = 0.1715(9)$ fm, determined from f_π in [45]. Column 4 gives the approximate value of a for each set. Column 5 gives the spatial (N_x) and temporal (N_t) dimensions of each lattice in lattice units and column 6, the number of configurations and time sources used in each case. Columns 7–11 give the masses of the valence and sea quarks in lattice units, noting that $m_u = m_d = m_l$ and the valence and sea masses are the same in the case of m_l . The valence s -quark masses are tuned to give $M_{\eta_s} = 0.6885(22)$ GeV [44,45]. We include the values of am_c^{val} in column 11, since this is always the lightest of the heavy-valence quark masses that we work with. A complete list of the heavy-quark masses used on each set is given in Table II. Column 12 shows values for the tensor normalization Z_T at scale $m_b = 4.8$ GeV ([42], Table VIII). Sets 1 and 2 did not include calculation of the tensor 3-point functions, so this is omitted in those cases.

Set	β	w_0/a	a (fm)	$N_x^3 \times N_t$	$n_{\text{cfg}} \times n_{\text{src}}$	$am_l^{\text{sea/val}}$	am_s^{sea}	am_c^{sea}	am_s^{val}	am_c^{val}	$Z_T(m_b)$
1	5.8	1.1367(5)	0.15	$32^3 \times 48$	998×16	0.00235	0.0647	0.831	0.0678	0.8605	...
2	6.0	1.4149(6)	0.12	$48^3 \times 64$	985×16	0.00184	0.0507	0.628	0.0527	0.643	...
3	6.3	1.9518(7)	0.088	$64^3 \times 96$	620×8	0.00120	0.0363	0.432	0.036	0.433	1.0029(43)
4	5.8	1.1119(10)	0.15	$16^3 \times 48$	1020×16	0.013	0.065	0.838	0.0705	0.888	0.9493(42)
5	6.0	1.3826(11)	0.12	$24^3 \times 64$	1053×16	0.0102	0.0509	0.635	0.0545	0.664	0.9740(43)
6	6.3	1.9006(20)	0.09	$32^3 \times 96$	499×16	0.0074	0.037	0.440	0.0376	0.449	1.0029(43)
7	6.72	2.896(6)	0.059	$48^3 \times 144$	413×8	0.0048	0.024	0.286	0.0234	0.274	1.0342(43)
8	7.0	3.892(12)	0.044	$64^3 \times 192$	375×4	0.00316	0.0158	0.188	0.0165	0.194	1.0476(42)

of our setup is shown in Fig. 1. An h “parent” quark propagator is generated as an “extended” propagator from a source at timeslice $t_0 + T$; the source is constructed from a light ‘spectator’ quark propagator originating from time

TABLE II. Masses in lattice units used for the valence heavy quarks on each set from Table I. The lightest heavy mass in each case corresponds to a well-tuned value for the charm quark mass [48]. m_h/m_c then reaches 4.1 on our finest lattices, set 8. Column 3 gives normalisation constants for the vector current from our results. Z_V is calculated using Eq. (6). Z_{disc} in column 4 is a small tree-level discretisation correction, beginning at $(am_h)^4$, that we make to all the matrix elements, see Eq. (10). It is defined in [49].

Set	am_h^{val}	Z_V	Z_{disc}
1	0.8605	1.0440(87)	0.99197
2	0.643	1.0199(54)	0.99718
3	0.433	1.0016(81)	0.99938
	0.683	1.011(10)	0.99648
	0.8	1.017(12)	0.99377
4	0.888	1.0376(52)	0.99050
5	0.664	1.0221(41)	0.99683
	0.8	1.0300(47)	0.99377
	0.9	1.0365(51)	0.99063
6	0.449	0.9977(67)	0.99892
	0.566	1.0033(80)	0.99826
	0.683	1.0091(85)	0.99648
	0.8	1.055(32)	0.99377
7	0.274	0.9901(94)	0.99990
	0.45	0.992(12)	0.99928
	0.6	0.996(13)	0.99783
	0.8	1.006(14)	0.99377
8	0.194	0.984(10)	0.99997
	0.45	0.993(12)	0.99928
	0.6	0.998(13)	0.99783
	0.8	1.006(16)	0.99377

slice t_0 . The h -quark propagator is combined with an s “daughter”-quark propagator from t_0 at time $t_0 + t$, where current J is inserted. The propagators are combined with appropriate color and spin (i.e. staggered spin taste) for the quantum numbers of a pseudoscalar to pseudoscalar transition via current J . Our calculation is set up in this “backwards” arrangement for computational convenience, as the physics is unchanged by a time reversal.

For each gluon-field configuration multiple values of t_0 , uniformly placed on the lattice, with the first being randomly selected to reduce autocorrelation, are used to increase our statistics. To improve the statistics on each ensemble further and to better fit the T dependence, multiple values of the source-sink separation T are also used for each t_0 value, with odd and even values included to capture oscillations in t . On most ensembles, we average the correlation functions for different t_0 values. On the finest ensemble (set 8), however, we do not do this. On this ensemble we have only four source t_0 values which are very

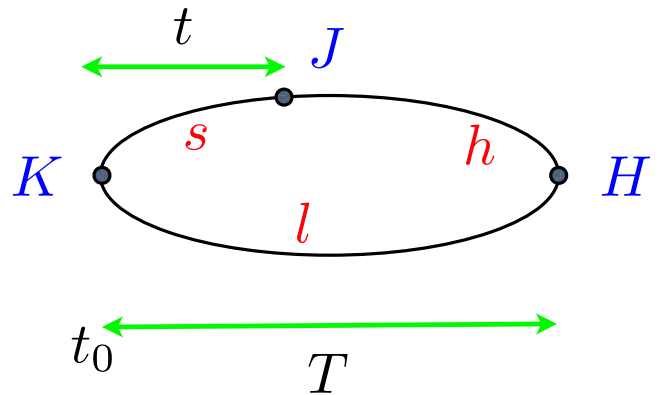


FIG. 1. Schematic of our three-point correlation function.

TABLE III. Details of the twists used for the K meson momenta on each gluon field ensemble. Momenta can be obtained from twist, θ , via $|a\vec{p}_K| = \theta(\sqrt{3}\pi)/N_x$, where N_x is the spatial dimension of the lattice in lattice units, given in Table I. \vec{p}_K is in the (1, 1, 1) direction. Column 3 gives the T values used for time extent, in lattice units, for the three-point correlation functions on each ensemble, see Fig. 1.

Set	θ	T
1	0, 2.013, 3.050, 3.969	9, 12, 15, 18
2	0, 2.405, 3.641, 4.735	12, 15, 18, 21
3	0, 0.8563, 2.998, 5.140	14, 17, 20
4	0, 0.3665, 1.097, 1.828	9, 12, 15, 18
5	0, 0.441, 1.323, 2.205, 2.646	12, 15, 18, 21
6	0, 0.4281, 1.282, 2.141, 2.570	14, 17, 20
7	0, 1.261, 2.108, 2.946, 3.624	20, 25, 30
8	0, 0.706, 1.529, 2.235, 4.705	24, 33, 40

widely spaced and tests confirm that correlations between them are negligible. It is then useful to keep the correlation functions for different t_0 as separate data to improve our determination of the covariance matrix.

The H meson is at rest on the lattice and momentum is given to the K meson. This momentum, \vec{p}_K , is generated in the (1, 1, 1) direction using twisted boundary conditions [50] for the s -quark propagator. The momentum in lattice units is related to the twist, θ , by $|a\vec{p}_K| = \theta(\sqrt{3}\pi)/N_x$, where N_x is the spatial extent of the lattice in lattice units. Different values of momentum are chosen so as to cover the full physical range of momentum transfer, q , on each lattice for the different heavy masses used. The corresponding twists are listed in Table III. Because we have a variety of heavy masses on each gluon-field ensemble, the coverage of the momenta cannot be optimized for each mass—we settle for values which give the best coverage overall. This means that some masses can generate negative q^2 values at large twist. Whilst these points are unphysical, they are easily accommodated in our fit form, as we shall see below.

As well as the aforementioned three-point functions, we also generate two-point correlation functions in the standard way for each of the H and K masses and momenta, in order to extract energies and amplitudes for the mesons.

In addition to the $H \rightarrow K$ results discussed above we also include results for $H_s \rightarrow \eta_s$ correlation functions from [32]. The $H_s \rightarrow \eta_s$ results are for sets 6 and 7 (called sets 1 and 2 in [32]) and include scalar and temporal vector current insertions in the three-point functions only. We do not include results on set 3 (set 8 here) from [32] as the statistics are much lower than for our $H \rightarrow K$ data, nor do we include the continuum $f_0(q_{\max}^2)$ data point used in that paper. The heavy masses and twists used there are the same as those used here and given in Tables I, III, and II. Instead of the spectator light quark that we have here, the earlier

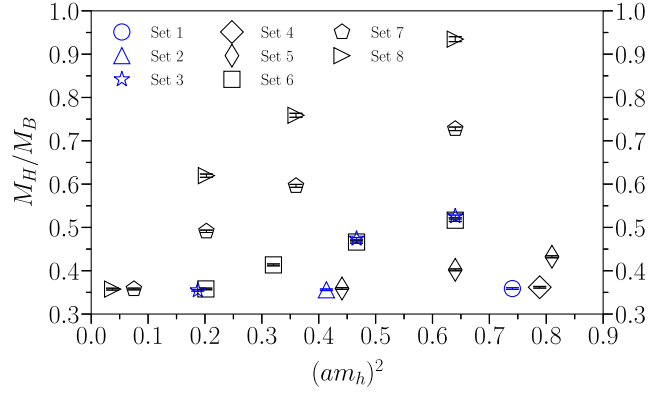


FIG. 2. The range of am_h values used in this work (Table II), and their corresponding M_H/M_B values. Ensembles with physical light quarks are shown in blue.

results have a spectator strange quark. For further details of the $H_s \rightarrow \eta_s$ data see [32]. The $H_s \rightarrow \eta_s$ data were fitted simultaneously with the $H \rightarrow K$ data on each of the two sets 6 and 7 in order to preserve correlations between the two. This helps us to pin down the chiral extrapolation for the spectator quark to the physical light mass by giving a third light-mass value: $m_l = m_s$, $m_l = m_s/5$ and $m_l \approx m_l^{\text{phys}}$. The effect of this extra light-mass value on the overall results will be discussed in Sec. III B.

Our ensembles contain a range of different am_h values (see Table II), as well as values for M_H/M_B which are correlated between the masses on a given ensemble. This is demonstrated in Fig. 2, and makes it possible for our fit to distinguish between am_h -dependent discretization effects and M_H dependence. In particular, all ensembles have data points at the physical charm mass, which differ only in their am_h values, and some am_h values, such as $am_h = 0.8$, are common to multiple ensembles with different M_H values. Additionally, the included $H_s \rightarrow \eta_s$ data discussed above provide an increased lever arm in the M_H dependence, via M_{H_s} , for a range of am_h values.

III. FITS AND ANALYSIS

A. Correlator fits

Using a standard Bayesian approach, as outlined in [51], we perform a simultaneous, multiexponential fit to both the two- and three-point correlation functions. This allows us to extract the ground-state energies, ground-state amplitudes and ground-state-to-ground-state current matrix elements with uncertainties that allow for any unresolved excited-state contamination. Fit quality is judged using χ^2 per degree of freedom (d.o.f.) values and the log of the Gaussian Bayes factor, $\log(\text{GBF})$. As discussed in [32] and the Appendix to [52], χ^2 values are artificially reduced by singular value decomposition (SVD) cuts and broad priors for the parameters. This means that χ^2 values should

not be taken at face value, but rather as a relative measure, comparable across fits where the SVD cut and priors are the same. The fitting packages we use [53–55] contain an in-built noise test [52], under which we check that our fits are stable and have an acceptable $\chi^2/\text{d.o.f.}$ value close to unity when appropriately modified by the inclusion of prior and SVD noise. The $\log(\text{GBF})$ value penalizes overfitting, so by also using this measure, we are able to confirm that our fits describe the data without overfitting.

We fit two-point correlators for a meson M to a set of exponentials representing a tower of possible states of energy E_i^M and amplitude d_i^M ,

$$C_2^M(t) = \sum_{i=0}^{N_{\text{exp}}} (|d_i^{M,n}|^2 (e^{-E_i^{M,n}t} + e^{-E_i^{M,n}(N-t)}) - (-1)^t |d_i^{M,o}|^2 (e^{-E_i^{M,o}t} + e^{-E_i^{M,o}(N-t)})). \quad (7)$$

The ground state is specified by $i = 0$. Because of the nature of staggered quarks, states which oscillate in time (labeled “o” as opposed to “n” for nonoscillating states) are also present and are accounted for in the fit. Discarding the first t_{min} data points allows us to fit to a finite number, N_{exp} , of exponentials, and t_{min} takes values in the range 2 to 7 for different correlators and different lattice spacings. We estimate priors for the ground-state energies and amplitudes using the effective mass and effective amplitudes, as in [32,36], and give each a broad uncertainty, ensuring that the final result of the fit is much more precisely determined than this prior. We use log-normal parameters throughout to enforce positive values on energy splittings and amplitudes. Amplitudes are guaranteed to be positive because we use the same interpolating operator at the source and sink. Priors for excited-state nonoscillating and all oscillating amplitudes are based on previous experience of amplitude sizes in similar fits [32,36]. Some priors are slightly adjusted by trial and error to maximize $\log(\text{GBF})$, as well as to ensure that the fit does not find spurious states, which have amplitudes consistent with zero but interfere with the ground-state determination. Priors for the oscillating ground-state energy of the H and K are taken to be 0.4 and 0.25 GeV larger than the nonoscillating ground states respectively, with prior widths on nonoscillating ground states typically in the range 2–10% and oscillating ground states 5–20%. In both cases prior widths vary by ensemble, and the posteriors are much better determined than their priors. The energy splitting between excited states is taken as 0.50(25) GeV. Other priors are listed in Table IV.

For the kaons with nonzero twist, as in [36], we use the dispersion relation to inform our ground-state priors, allowing for discretization effects using the following ansatz:

TABLE IV. Priors used in the fit on each set. Priors are based on previous experience and given large widths. Sometimes, initial priors are tightened or loosened in order to find a fit with an acceptable χ^2 . These changes are balanced against the resulting change in $\log(\text{GBF})$ (see text). On rare occasions, the fit finds spurious states (with zero amplitude). This renders the fit very obviously wrong, and is easily remedied with an adjustment to the offending priors. The effect of doubling and halving the standard deviation on all priors on the final fit result is shown in Fig. 3. $d_{i \neq 0}^M$ indicates the amplitudes for oscillating and nonoscillating H mesons and for nonoscillating kaons. $d_i^{K,o}$ is the amplitude for oscillating kaons, which we expect to be smaller, particularly in the case of zero momentum. $P[S_{ij \neq 0}^{kl}] = P[V_{ij \neq 0}^{0,kl}] = 0.0(5)$ and $P[V_{ij \neq 0}^{1,kl}] = P[T_{ij \neq 0}^{kl}] = 0.0(1)$ in all cases, whilst $P[V_{00}^{1,kl \neq nn}] = 0.0(3)$.

Set	$P[d_{i \neq 0}^M]$	$P[d_i^{K,o}]$	$P[S_{00}^{kl \neq nn}]$	$P[V_{00}^{0,kl \neq nn}]$	$P[T_{00}^{kl \neq nn}]$
1	0.15(20)	0.05(5)	0.0(1.0)	0.0(1.0)	...
2	0.15(10)	0.05(5)	0.0(1.0)	0.0(1.0)	...
3	0.10(10)	0.05(5)	0.0(1.5)	0.0(1.5)	0.0(3)
4	0.20(20)	0.05(5)	0.0(1.0)	0.0(1.0)	0.0(3)
5	0.20(20)	0.03(3)	0.0(1.0)	0.0(1.5)	0.0(3)
6	0.10(10)	0.05(5)	0.0(1.5)	0.0(1.5)	0.0(3)
7	0.05(5)	0.02(2)	0.0(1.0)	0.0(2.0)	0.0(3)
8	0.08(10)	0.01(2)	0.0(1.0)	0.0(2.0)	0.0(2)

$$P[aE_{0,\vec{p}}^{K(\wedge)}] = \sqrt{P[aE_{0,0}^{K(\wedge)}]^2 + (a\vec{p})^2} \left(1 + P[c_2] \left(\frac{a\vec{p}}{\pi} \right)^2 \right),$$

$$P[d_{0,\vec{p}}^{K(\wedge)}] = \frac{P[d_{0,0}^{K(\wedge)}]}{\left[1 + (a\vec{p}/P[aE_{0,0}^{K(\wedge)}])^2 \right]^{1/4}} \left(1 + P[d_2] \left(\frac{a\vec{p}}{\pi} \right)^2 \right). \quad (8)$$

Here $P[d]$ and $P[aE]$ represent the priors of the relevant amplitudes and energies. We take priors for c_2 and d_2 as 0 ± 1 based on observations of dispersion relations in similar fits [25,32,36]. We find their posteriors to fall comfortably within their priors in all fits, typically with a magnitude less than 0.5.

We perform three-point fits (for mother and daughter mesons M_2 and M_1) with scalar, vector and tensor current insertions to the following form:

$$C_3^{M_1, M_2}(t, T) = \sum_{i,j=0}^{N_{\text{exp}}} (d_i^{M_1,n} J_{ij}^{\text{nn}} d_j^{M_2,n} e^{-E_i^{M_1,n}t} e^{-E_j^{M_2,n}(T-t)} - (-1)^{(T-t)} d_i^{M_1,n} J_{ij}^{\text{no}} d_j^{M_2,o} e^{-E_i^{M_1,n}t} e^{-E_j^{M_2,o}(T-t)} - (-1)^t d_i^{M_1,o} J_{ij}^{\text{on}} d_j^{M_2,n} e^{-E_i^{M_1,o}t} e^{-E_j^{M_2,n}(T-t)} + (-1)^T d_i^{M_1,o} J_{ij}^{\text{oo}} d_j^{M_2,o} e^{-E_i^{M_1,o}t} e^{-E_j^{M_2,o}(T-t)}). \quad (9)$$

Here J_{ij}^{kl} ($i, j \in \{0, 1, \dots, N_{\text{exp}} - 1\}$, and $k, l \in \{\text{n}, \text{o}\}$) are matrix elements of $J = S(V)[T]$ for the scalar (vector) [tensor] currents. For example, J_{ij}^{no} , gives the matrix element for J between the i th nonoscillating (n) state of M_1 and the j th oscillating (o) state of M_2 . T and t appear as in Fig. 1 (where we have taken $t_0 = 0$), and T is not to be confused with the tensor current insertion. The key parameters that we want to determine are the J_{00}^{nn} for each current.

Priors for J_{00}^{nn} are estimated by dividing the three-point correlation function by the relevant two-point correlators and multiplying by their effective amplitudes (as in [32,36]). A broad uncertainty (typically 20–50%) is then given to this effective amplitude. Other J_{ij}^{kl} priors are listed in Table IV.

On each ensemble, using the CORRFITTER package, [53–55], we perform a simultaneous fit to all of the two-point and three-point functions for all $a\vec{p}_K$ and T values, selecting N_{exp} for each lattice spacing such that it gives an acceptable χ^2 and maximizes the $\log(\text{GBF})$. We use $N_{\text{exp}} = 4$ for all ensembles except set 8 where we use $N_{\text{exp}} = 5$. In the case of sets 6, 7 and 8, the fits are very large because of the number of heavy masses and twists, as well as the increasing number of time slices. To handle this, we split them up, fitting each heavy mass sequentially and taking a correlated weighted average of any shared parameters at the end. This is especially necessary in the case of sets 6 and 7, where combining the $H_s \rightarrow \eta_s$ data with the $H \rightarrow K$ data as described in Sec. II C makes the fits even larger. Tests across the range of J , \vec{p}_K and m_h show that this method preserves correlations between J_{00}^{nn} very well. These correlations are small, typically less than 0.3.

Since our fits involve a large number of different correlation functions with a finite number of samples there is a bias in the small eigenvalues of the covariance matrix. We address this by applying an SVD cut to these eigenvalues; see Appendix D of [52]. This is a conservative move which increases errors. As discussed above, it also leads to an artificial reduction in χ^2 , something which we check for by introducing SVD noise, again using CORRFITTER (see documentation for further details [53–55]).

We check stability of our fitted results for the ground-state parameters to a variety of changes to the fit. An illustration of such tests is given in Fig. 3 for set 8, showing the results for the ground-state-to-ground-state tensor current matrix element at one twist value at one heavy-quark mass along with the ground-state \hat{H} -meson mass at a different heavy-quark mass and the ground-state K -meson energy for a different twist (thus showing a broad range of results). A stability plot for a lower mass (m_c) on set 5 with the vector current matrix element is given in [36]. We check stability against changing the number of excited states included, doubling and halving all of the prior widths, doubling and halving the SVD cut (compared to the recommended cut given by the LSQFIT

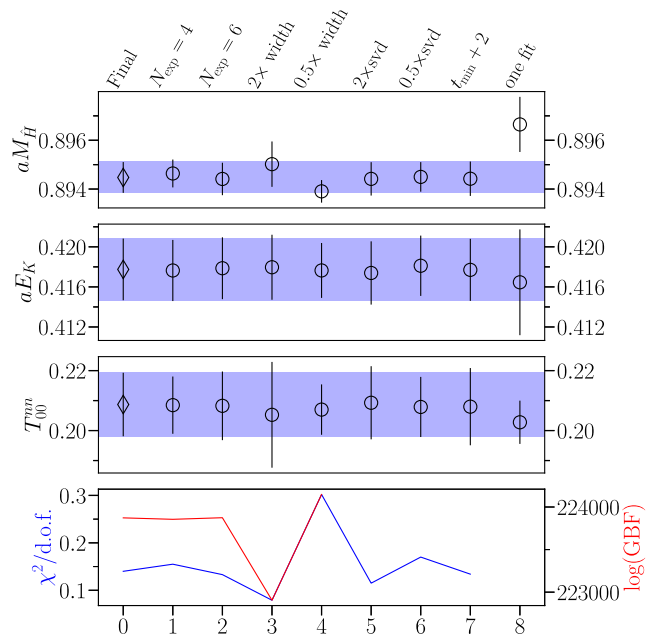


FIG. 3. Stability plot for different correlator fit choices on set 8, showing the mass of the ground-state non-Goldstone \hat{H} meson for $am_h = 0.6$, the ground-state energy of the K with twist $\theta = 4.705$ and T_{00}^{nn} for $am_h = 0.45$, $\theta = 2.235$. Test 0 is the final result, corresponding to $N_{\text{exp}} = 5$ exponentials. Tests 1 and 2 use one fewer and one more exponential respectively. Tests 3–6 double and halve the prior widths and SVD cut. Test 7 increases t_{min} by 2 across the whole fit. The final test, 8, is when the fit is done on its own, or in the case of the T_{00}^{nn} , just with the \hat{H} and \hat{K} two-point correlators required, as opposed to being part of one big simultaneous fit. The χ^2 per degree of freedom and $\log(\text{GBF})$ value for each test are shown in the bottom pane in blue and red respectively. For the later tests (5–7), data are removed from the fit, resulting in a lower $\log(\text{GBF})$ which is not comparable with the others and not displayed. As discussed in Sec. III A, χ^2 values are artificially lowered by our SVD cut and priors so are only meaningful relatively. χ^2 values for tests 3–6, which change prior width and SVD, are thus not directly comparable with other tests. The final fit gives a $\chi^2/\text{d.o.f.}$ close to 1 with SVD and prior noise.

package [53]) and changing t_{min} . We also show the result of doing a single fit, rather than a simultaneous fit to multiple correlators. This figure aims to give a representative range of examples on one ensemble; other ensembles were similarly well behaved, showing stable fits in all cases. We also check that the momentum-dispersion relation for our \hat{K} fit results agrees with the twists specified in the lattice calculation. The two should differ by discretization effects only and this is confirmed in [36] which uses the same kaon data on all ensembles as here. We can also infer this from the modest values we find for c_2 and d_2 from Eq. (8) in all cases.

Our fit parameters J_{00}^{nn} are converted into matrix elements for the corresponding lattice currents according to

$$\langle K | J_{\text{latt}} | H \rangle = 2Z_{\text{disc}} \sqrt{M_H E_K} J_{00}^{\text{nn}}. \quad (10)$$

These matrix elements can then be converted into values for the form factors using Eqs. (1), (2), and (3). We have included a factor Z_{disc} to account for small ($\mathcal{O}(am_h)^4$) tree-level discretization effects. Values for Z_{disc} are given in Table II. We always use the mass of the Goldstone H pseudoscalar for the conversion as the non-Goldstone mass is the same in the continuum limit. The difference is a small discretization effect, less than 0.1% in [36], which is accounted for in our extrapolation to the physical point (Sec. III B).

Numerical results for the left-hand side of Eq. (10) on each of our ensembles are summarized in Tables X, XI, and XII in Appendix C. The vector current results must be multiplied by values of Z_V from Table II and the tensor current results by values of Z_T from Table I before values for the form factors can be obtained. The form factor values are also given in the tables in Appendix C.

B. Extrapolating form factors using a modified z expansion

Once we have our form factors over a range of q^2 values and on all ensembles, we perform a fit in q^2 space, heavy mass, light-quark mass and lattice spacing. We can then evaluate our form factors at the physical quark masses, and zero lattice spacing, at any heavy-light meson mass from the physical D mass to the physical B mass. Following the method successfully employed in [32,35,36], we fit the form factors on the lattice using the Bourreley-Caprini-Lellouch (BCL) parametrization [56],

$$\begin{aligned} f_0(q^2) &= \frac{\mathcal{L}}{1 - \frac{q^2}{M_{H_s^*}^2}} \sum_{n=0}^{N-1} a_n^0 z^n \\ f_+(q^2) &= \frac{\mathcal{L}}{1 - \frac{q^2}{M_{H_s^*}^2}} \sum_{n=0}^{N-1} a_n^+ \left(z^n - \frac{n}{N} (-1)^{n-N} z^N \right) \\ f_T(q^2) &= \frac{\mathcal{L}}{1 - \frac{q^2}{M_{H_s^*}^2}} \sum_{n=0}^{N-1} a_n^T \left(z^n - \frac{n}{N} (-1)^{n-N} z^N \right). \end{aligned} \quad (11)$$

This uses a mapping of q^2 to z , so that the physical q^2 range $0 \leq q^2 \leq (M_H - M_K)^2$ is mapped to a region within the unit circle in z :

$$z(q^2, t_0) = \frac{\sqrt{t_+ - q^2} - \sqrt{t_+ - t_0}}{\sqrt{t_+ - q^2} + \sqrt{t_+ - t_0}}. \quad (12)$$

$t_+ = (M_H + M_K)^2$ is the beginning of a branch cut in the complex $t = q^2$ plane corresponding to HK production in the crossed channel. We choose to take $t_0 = 0$, which

permits a simple enforcement of the kinematic constraint in Eq. (4) as it means $z(q^2 = 0) = 0$. Fit results were compared for different values of t_0 in [36] and good agreement was found.

The first term in the fit forms of Eq. (11) removes poles in the form factor that appear from production of heavy-strange mesons with squared masses below t_+ (but above t_-). These mesons are the scalar H_{s0}^* and vector H_s^* states. In our fits we need to use a mass for these mesons that is simply related to masses that we have measured in our calculation. We take $M_{H_{s0}^*}$ to be $M_H + \Delta$ with $\Delta = 0.45$ GeV. As discussed in [32] the exact value used here is unimportant. The value of Δ is taken from experimental results for the D system; there are no experimental results for the B system but we expect the splitting to be largely independent of m_h . The vector mass $M_{H_s^*}$ can be estimated, as in [32,35], with the PDG [57] values $M_{D_s^*}^{\text{phys}} = 2.1122(4)$ GeV, $M_{B_s^*}^{\text{phys}} = 5.4158(15)$ GeV. We use

$$\begin{aligned} M_{H_s^*} &= M_H + \frac{M_D^{\text{phys}}}{M_H} \Delta(D) + \frac{M_B^{\text{phys}}}{M_H} \left(\frac{M_H - M_D^{\text{phys}}}{M_B^{\text{phys}} - M_D^{\text{phys}}} \right) \\ &\quad \times \left(\Delta(B) - \frac{M_D^{\text{phys}}}{M_B^{\text{phys}}} \Delta(D) \right), \end{aligned} \quad (13)$$

where $\Delta(H) = M_{H_s^*}^{\text{phys}} - M_H^{\text{phys}}$. The physical masses used are those for the isospin averages $(K^0 + K^\pm)/2$, $(B^0 + B^\pm)/2$ and $(D^0 + D^\pm)/2$ (all from [57]), corresponding to the fact that our lattice results have $m_u = m_d = m_l$. We also need to consider isospin breaking effects and we will do this below.

The form factor, with sub-threshold poles removed, can be expanded as an order N polynomial in z , where $z < 1$ for the physical region. On the lattice the coefficients of z^n in Eq. (11) contain discretisation effects, which appear as powers of the squared lattice spacing for the HISQ action. Since we are fitting results for multiple values of the heavy quark mass here the coefficients will carry dependence on the heavy quark mass. We must also allow for dependence on the light quark (spectator and sea quark mass) and we do this using a chiral logarithm factor \mathcal{L} as well as analytic terms. For each form factor and each power, n , of z we take

$$\begin{aligned} a_n^{0,+T} &= \left(\frac{M_D}{M_H} \right)^{\zeta_n} \left(1 + \rho_n^{0,+T} \log \left(\frac{M_H}{M_D} \right) \right) \times (1 + \mathcal{N}_n^{0,+T}) \\ &\quad \times \sum_{i,j,k,l=0}^{N_{ijkl}-1} d_{ijkln}^{0,+T} \left(\frac{\Lambda_{\text{QCD}}}{M_H} \right)^i \left(\frac{am_h^{\text{val}}}{\pi} \right)^{2j} \\ &\quad \times \left(\frac{a\Lambda_{\text{QCD}}}{\pi} \right)^{2k} (x_\pi - x_\pi^{\text{phys}})^l \end{aligned} \quad (14)$$

and will discuss the different pieces of this expression below. Note that the coefficients for each power of z are independent in our fit.

1. Discretisation effects

Discretisation effects are accounted for in two ways in Eq. (14). We allow for discretisation effects that vary with the heavy quark mass through the terms in am_h with power $2j$. The size of these terms will vary between results for different m_h on a given ensemble. Discretisation effects that do not vary with heavy quark mass but instead are set by some other scale (for example associated with the K mesons) are allowed for in the powers of $a\Lambda_{\text{QCD}}$. These terms will be the same for all heavy quark masses on a given ensemble. We take $\Lambda_{\text{QCD}} = 0.5$ GeV.

We also consider the possibility of logarithmic cutoff effects [58] via the addition of an $(am_h)^2 \log(am_h)$ term, discussed in Sec. III B 6.

2. Dependence on heavy quark mass

We include several terms in Eq. (14) to model the physical dependence of the form factors on heavy quark mass, using as a proxy for this the heavy-light meson mass, M_H . This dependence connects the form factors for $D \rightarrow K$ to those for $B \rightarrow K$ and we can use insights from Heavy Quark Effective Theory (HQET) to suggest a functional form for it. We take a power series in inverse powers of M_H (with power i and Λ_{QCD} as above) multiplying a prefactor $(M_D/M_H)^{\zeta_n}$, with fitted power ζ_n , and a logarithmic term. The $(M_D/M_H)^{\zeta_n}$ term models behaviour predicted by Large Energy Effective Theory (LEET) [59]. The LEET expectation is for all form factors for a specific heavy to light transition to exhibit common $\sim M_H^{-3/2}$ behaviour in the region of $q^2 = 0$ (where the light meson energy is close to $M_H/2$). This behaviour was observed in lattice QCD results for the closely related $B_s \rightarrow \eta_s$ decay [32], with an M_H power between -1.5 and -1 towards $q^2 = 0$. In that case the behaviour was modelled with a $\log(M_{D_s}/M_{H_s})$ term multiplied by a series in inverse powers of M_H . Here we allow for this behaviour explicitly.

Because we have taken $t_0 = 0$, the form factors at $q^2 = 0$ are set by the z^0 terms in the z -expansion. We therefore take a prior $P[\zeta_0] = 1.5(5)$ as a common prior for the a_0 coefficients but set $\zeta_{n \neq 0} = 0$ for the other a_n . M_K/M_H corrections to LEET can be accounted for in the form factor dependent $(\Lambda_{\text{QCD}}/M_H)^i$ terms in our fit, as $M_K \approx \Lambda_{\text{QCD}}$. We find that including this term in our fit increases log(GBF), reduces uncertainty at $q^2 = 0$, particularly for f_T , and returns a posterior of $\zeta_0 = 1.43(12)$. Allowing a broader prior $P[\zeta_0] = 1.0(1.0)$ returns a posterior consistent with 1.5 (1.42(12)) and does not change the form factor result. Allowing ζ_0 to vary between form factors simply increases the uncertainty on $f_T(0)$, whilst leaving the central values unchanged. These tests confirm that our

fit is not overly constrained by ζ and is flexible with regard to M_H dependence. They will be discussed further in Sec. III B 6, along with a test allowing $\zeta_{n \neq 0}^{0,+T} \neq 0$.

For both the $n = 0$ and the $n \neq 0$ coefficients we include the logarithmic term in Eq. (14), with priors on ρ_n of 0.0(1.0). This term is motivated by the matching of HQET to QCD, as in [32,35]. For $n = 0$ this effectively allows for different form factors to have different powers ζ as well as allowing for sub-leading M_H dependence from LEET [59]. For $n \neq 0$ this term allows for an adjustable pre-factor non-integer power of M_H for different dependence on M_H in different regions of the q^2 range. The heavy mass dependence of the continuum form factors will be discussed below in Sec. IV C.

3. Dependence on spectator quark mass

The dependence of the form factors on spectator quark mass is also a physical effect which connects $B \rightarrow K$ form factors (with a light spectator quark) smoothly to those for $B_c \rightarrow D_s$ [38] (with a charm spectator quark). We will discuss this comparison in Sec. IV. Here we include spectator quark masses varying from the physical value of m_l up to m_s (the latter corresponding to $B_s \rightarrow \eta_s$ form factors) in our dataset and aim to describe them all with our functional dependence on the spectator quark mass. This region of spectator masses is amenable to chiral perturbation theory [60] and we use this to fix the chiral logarithm term, \mathcal{L} in Eq. (14). We also include analytic terms to be discussed below. \mathcal{L} takes the form

$$\mathcal{L} = 1 - \frac{9g^2}{8} x_\pi (\log x_\pi + \delta_{FV}) - \left(\frac{1}{2} + \frac{3g^2}{4} \right) x_K \log x_K - \left(\frac{1}{6} + \frac{g^2}{8} \right) x_\eta \log x_\eta, \quad (15)$$

where $x_{\mathcal{M}} = \frac{M_{\mathcal{M}}^2}{(4\pi f_\pi)^2}$ and g is the coupling between H , H^* and the light mesons. The form of \mathcal{L} is appropriate for the vector and scalar form factors and, as in [61], we make use of the fact that f_T and f_+ in HQET are the same up to $\mathcal{O}(1/M_H)$ terms to use the same \mathcal{L} for the tensor form factor. Any corrections to this are easily absorbed by our HQET expansion. In fact \mathcal{L} does not have a big impact on our fit and we find no appreciable difference to the fit if we set $\mathcal{L} = 1$ (see Sec. III B 6).

x_π in Eq. (15) is constructed from the meson mass for a pseudoscalar meson made from the spectator quarks. This corresponds to the π meson for the $B \rightarrow K$ case (albeit with an unphysically heavy light quark on some ensembles) but an η_s meson in the $B_s \rightarrow \eta_s$ case. Likewise x_K corresponds to a “ K ” meson constructed from a strange quark and a spectator quark. The value of M_η appearing in x_η is given by $M_\eta^2 = (M_\pi^2 + 2M_{\eta_s}^2)/3$. Since not all of these meson masses are available in our calculation we use leading-order chiral perturbation theory to rescale meson masses in

proportion to the masses of the quarks they contain. Taking the ratio of $4\pi f_\pi$ to $M_{\eta_s}^{\text{phys}} = 0.6885(22)$ GeV [45], we use a proxy for x_π of the form

$$x_\pi \approx 2 \frac{m_{\text{spectator}}}{5.63 m_s}, \quad (16)$$

where the factor of 2 accounts for the definition of f_π^2 in [60]. x_K and x_η are constructed in an analogous way. The finite volume correction, δ_{FV} , adjusts the π chiral logarithm (Eq. 47 of [62]), and we include an error of $(0.7\%)^2$ to account for higher order terms.

In order to capture the heavy mass dependence of g , we take

$$g(M_H) = g_\infty + C_1 \frac{\Lambda_{\text{QCD}}}{M_H} + C_2 \frac{\Lambda_{\text{QCD}}^2}{M_H^2}, \quad (17)$$

with $g_\infty = 0.48(11)$ [63], $g(M_D) = 0.570(6)$ [64] and $g(M_B) = 0.500(33)$, an average of the values in [65–67]. Priors $P[C_1] = 0.5(1.0)$ and $P[C_2] = 0.0(3.0)$ are broad and based on a trial fit to just the g data points given above. Our final fit has a slightly tighter value for g_∞ giving posterior $g_\infty = 0.457(56)$ with coefficients $C_1 = 0.73(62)$ and $C_2 = -1.2(1.7)$.

As well as the chiral logarithm term \mathcal{L} that is common to all terms in the z -expansion, we include analytic terms in the spectator quark mass that can vary for different form factors and with the power of z , n . These appear through powers of $(x_\pi - x_\pi^{\text{phys}})$ in Eq. (14) (with power l). x_π^{phys} is defined as for x_π in Eq. (16) and using

$$\frac{m_s^{\text{phys}}}{m_l^{\text{phys}}} = 27.18(10) \quad (18)$$

from [68].

We will quote our final form factors at the physical value of m_l i.e. at the average of the physical u and d quark masses. We will discuss tests of isospin-breaking effects in Sec. III B 6 below.

4. Mistuning effects for other quark masses

We must also account for any possible mistuning of the strange daughter quark and for mistuning of the quark masses in the sea. These are wrapped up in the quark mass-mistuning term, \mathcal{N} , in Eq. (14). The mass of the strange daughter quark is always the valence s quark mass, listed in Table I. We take

$$\begin{aligned} \mathcal{N}_n^{0,+T} = & c_{s,n}^{\text{val},0,+T} \delta_s^{\text{val}} + c_{s,n}^{\text{sea},0,+T} \delta_s^{\text{sea}} + 2c_{l,n}^{\text{sea},0,+T} \delta_l \\ & + c_{c,n}^{\text{sea},0,+T} \delta_c^{\text{sea}} \end{aligned} \quad (19)$$

For the s and l quarks we use:

$$\delta_q = \frac{m_q - m_q^{\text{tuned}}}{10m_s^{\text{tuned}}}. \quad (20)$$

Dividing by m_s^{tuned} here makes this a physical, scale-independent ratio and the factor of 10 matches this approximately to the usual expansion parameter in chiral perturbation theory. As discussed in Sec. II C, our valence s quark masses are all well-tuned using the physical value of the η_s mass to derive m_s^{tuned} [44,45]; this is less true for the sea s quarks. We include uncertainties in m_s^{tuned} by defining it from the η_s masses corresponding to our valence s quark masses through

$$m_s^{\text{tuned}} = m_s^{\text{val}} \left(\frac{M_{\eta_s}^{\text{phys}}}{M_{\eta_s}} \right)^2. \quad (21)$$

m_l^{tuned} is then defined from Eq. (18). For the sea charm quarks we define

$$\delta_c^{\text{sea}} = \frac{m_c^{\text{sea}} - m_c^{\text{tuned}}}{m_c^{\text{tuned}}} \quad (22)$$

with m_c^{tuned} fixed from the η_c meson mass [48]. These values, on each ensemble, correspond well with the lowest heavy valence mass that we have used (see Table II).

5. Prior choices

We need to set priors for the parameters that appear in the a_n coefficients of Eq. (14). As noted in Sec. III B 2 we include a parameter for an inverse power of M_H as a prefactor for $n = 0$ only, and take the prior for ζ_0 as $1.5(5)$. For ρ_n and d_{ijkln} we take values of $0.0(1.0)$ in all cases except for terms which are $\mathcal{O}(a^2)$. We know such terms are highly suppressed in the HISQ action because it is a^2 -improved [27], so we take a reduced width prior of $0.0(0.3)$ for d_{i10ln} and d_{i01ln} terms. Using such priors, we test the fit with different choices of $N_{ijkl} \equiv (N_i, N_j, N_k, N_l)$, and we find that the combination preferred by $\log(\text{GBF})$ is $N_{ijkl} = (3, 2, 2, 3)$. Note that the sum over each index, i , runs from 0 to $N_i - 1$ in Eq. (14). We show below in Sec. III B 6 that increasing all of the entries in N_{ijkl} by 1 makes almost no difference to the final results.

We also conduct an Empirical Bayes study in order to confirm that the priors listed above are of the right size. We do this using the facility built into `lsqfit` [53]. It works by varying a factor w which multiplies all prior widths (or a subset of them) in order to find the w choice which maximises $\log(\text{GBF})$. In our case, we perform two such studies, on the whole set of $0.0(1.0)$ and $0.0(0.3)$ priors respectively. We find that our priors are conservative in both cases, with priors of $0.00(55)$ and $0.000(72)$ giving the optimal $\log(\text{GBF})$. Taking these priors results in a $\log(\text{GBF})$ increase of ≈ 2 , which is not considered to be very significant, so we opt for our original, more conservative priors. The effect of doubling and halving the priors will be shown in Fig. 4, discussed in Sec. III B 6.

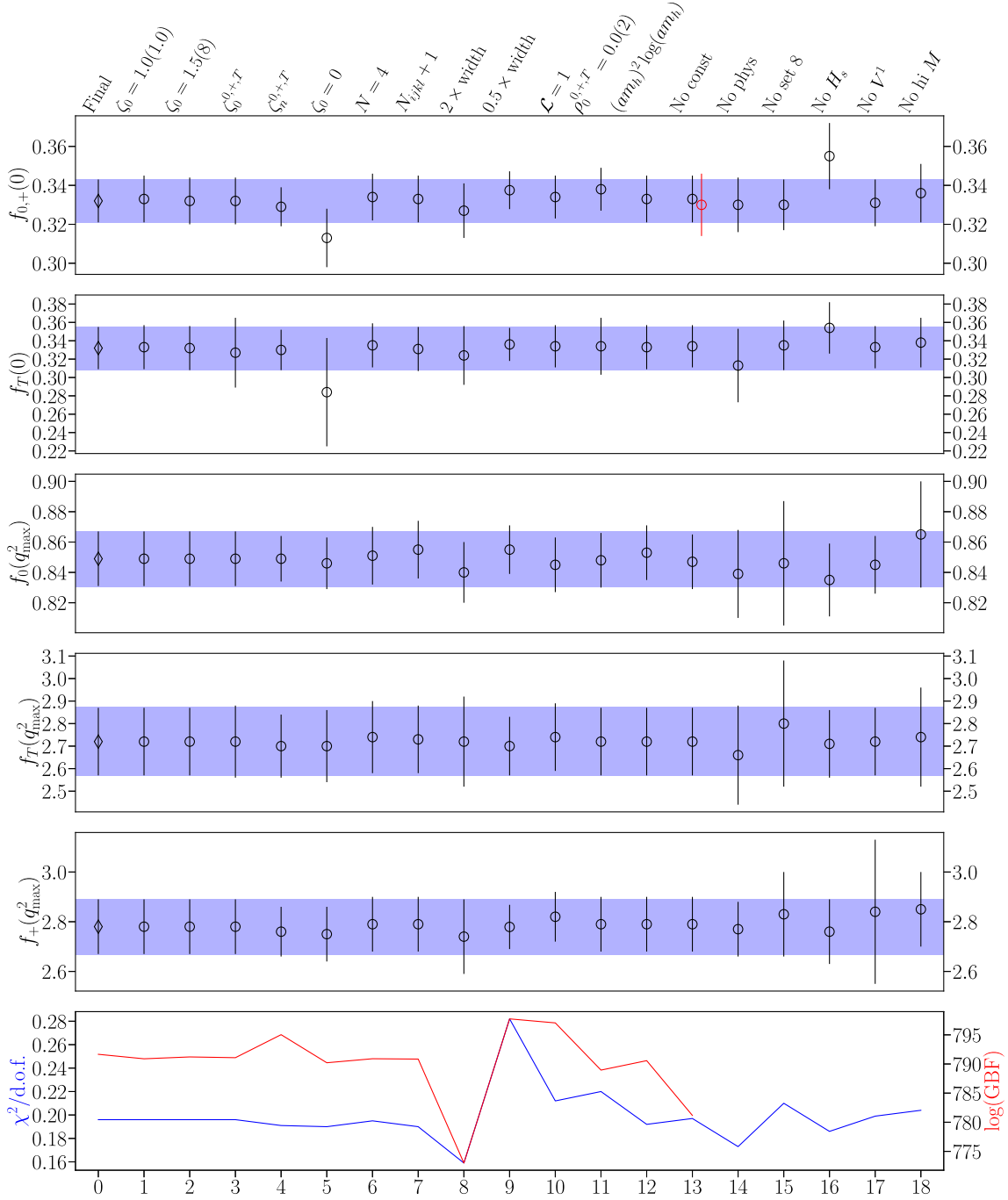


FIG. 4. Stability tests for the z -expansion fit evaluated at the physical B mass. Test 0 is the final result, 1 and 2 take different priors for ζ_0 , test 3 allows ζ_0 to vary between the form factors and test 4 (see text) allows for $\zeta_{n \neq 0} \neq 0$. Test 5 drops the term containing ζ entirely. Test 6 increases the number of the terms in the z expansion, N , by 1 (to 4) and test 7 does the same for each component of N_{ijkl} in each a_n coefficient. Test 8 doubles the width of ζ_n and all d and ρ priors, and 9 halves them. Test 10 removes the chiral logarithm term by setting $\mathcal{L} = 1$, and 11 tightens the prior on the ρ coefficients considerably. Test 12 allows for logarithmic heavy-mass dependence $(am_h)^2 \log(am_h)$ in the fit. Test 13 removes the $f_0(0) = f_+(0)$ constraint; in this case the black point is $f_0(0)$ and the red is $f_+(0)$. Tests 14, 15 and 16 remove all the lattices with physical light masses, all of set 8 data, and results with $m_l = m_s$ respectively. Test 17 removes the spatial vector data, and 18 removes the largest mass from all ensembles with multiple masses. The χ^2 per degree of freedom and $\log(\text{GBF})$ value for each test are shown in the bottom panel in blue and red respectively. For the latter tests, data are removed from the fit, resulting in a lower $\log(\text{GBF})$ which is not comparable with others and so not displayed. As in our correlator fits, χ^2 values are artificially lowered by our SVD cut and priors so are only meaningful relatively. χ^2 values for tests 7 and 8, which change widths on many priors, are thus not directly comparable with other tests. No SVD cut is required, and our final fit has a $\chi^2/\text{d.o.f.}$ of 0.3 when prior noise is included.

The prior for the daughter strange quark mistuning parameter in \mathcal{N} , $c_{s,n}^{\text{val}}$, is taken as 0.0(1.0) for each n and each form factor. This size is based on the variation seen between $B \rightarrow K$ and $B \rightarrow \pi$ form factors [20]. We expect smaller effects from sea quark mass mistuning and so take the $c_{s,n}^{\text{sea}}$ and $c_{l,n}^{\text{sea}}$ parameters to have priors of 0.0(0.5) and the $c_{c,n}^{\text{sea}}$ parameters to have prior 0.0(1).

The choice of $t_0 = 0$ and the use of $x_\pi - x_\pi^{\text{phys}}$ (which takes value 0 at the physical point) in Eq. (14) makes it easy to apply the constraint that $f_+(0) = f_0(0)$ at the physical point for all heavy masses [Eq. (4)]. We achieve this by setting $\rho_0^+ = \rho_0^0$ and $d_{i0000}^+ = d_{i0000}^0$. We take $N = 3$ in Eq. (11) so that the maximum power of z corresponding to a fit parameter in the z -expansion is z^2 . We show below in Sec. III B 6 that increasing N by 1 makes no appreciable difference to the final results.

6. Tests of the fits

We perform a variety of tests of the stability of our fits and these are summarised in Fig. 4. This shows how the final $B \rightarrow K$ form factors at each end of the q^2 range (0 and q_{max}^2) vary as we change fit choices. Figure 4 demonstrates that our preferred fit result is stable against reasonable variations and simultaneously optimises $\log(\text{GBF})$ and $\chi^2/\text{d.o.f.}$. The only variations with a larger $\log(\text{GBF})$ than our preferred fit are those which set $\mathcal{L} = 1$ (test 10) and which halve the prior widths on ζ_0 and all d and ρ parameters. However, \mathcal{L} is theoretically motivated and we prefer to keep more conservative priors. Our final fit has an acceptable $\chi^2/\text{d.o.f.}$ (0.3) when prior noise is included. No SVD cut is used in the fit.

Tests 1–5 address variations of the power ζ_0 of M_H in the pre-factor term for the heavy-quark expansion in Eq. (14). Tests 1 and 2 change the prior for ζ_0 , whilst test 3 allows ζ_0 to vary between form factors. Test 4 examines the effect of introducing ζ away from $q^2 = 0$. We take the usual correlated prior $\mathcal{P}[\zeta_0] = 1.5(5)$, but allow uncorrelated priors for each of the form factors for $n \neq 0$: $\mathcal{P}[\zeta_{n \neq 0}^0] = 1.5(5)$ and $\mathcal{P}[\zeta_{n \neq 0}^{+,T}] = 0.5(5)$. This allows approximately for the expected scaling at q_{max}^2 from HQET [69], allowing for the single power of M_H from the pole term. This is discussed in more detail below (Sec. IV C). The scaling is not perfectly accounted for, as we are working in z space, but we find that the output of the fit agrees very well with our preferred result, and indeed has smaller uncertainties, smaller $\chi^2/\text{d.o.f.}$ and larger $\log(\text{GBF})$. We do not wish to constrain our fit so tightly, however, so we take the more conservative approach of only using ζ_0 . Test 5 drops this ζ term entirely.

Test 6 adds additional z^3 terms to the z -expansion and test 7 adds additional discretisation, heavy quark expansion and m_l terms to each a_n . These do not change the fit output in any appreciable way. Tests 8 and 9 double and halve, respectively, the prior widths on ζ_0 and all d and ρ priors.

Again these make little difference, but we note that the $\log(\text{GBF})$ grows for the case of smaller widths, indicating that our choice is conservative, as discussed in Sec. III B 5. Test 10 drops the chiral logarithm term, \mathcal{L} and we see little difference in this case as noted in Sec. III B 3. The analytic terms included in the a_n are then capable of modelling the dependence that we see for the range of spectator quark masses that we have.

In test 12, we allow for logarithmic terms $(am_h)^2 \log(am_h)$ in the heavy mass [58]. We do this by including a term $(1 + \omega_n^{0,+T} \log(am_h))$ in Eq. (14) when $j = 1$ with prior $\mathcal{P}[\omega_n^{0,+T}] = 0(1)$. We find that the posteriors returned are consistent with zero, and the final form factors are not changed significantly.

With test 13 we show that removing the constraint of Eq. (4) also has little effect beyond a slightly larger uncertainty for f_+ at $q^2 = 0$.

The tests from 14 upwards miss out various sets of data from the fit and some of these have a sizeable impact on the uncertainties. Dropping the results with the highest heavy quark mass from each ensemble (test 18), unsurprisingly increases the uncertainties considerably at q_{max}^2 since these results are the ones closest to the b quark (and therefore closest to the physical q_{max}^2 for $B \rightarrow K$). This is also reflected in the contribution to the error budget from the HQET part of the expansion of the a_n . This will be discussed in Sec. IV.

Dropping all the results from our finest lattice, set 8, also has a significant effect on uncertainties (test 15) because this set allows us to get closest to the b mass. The gluon field ensembles on set 8 show only a slow variation of topological charge in Monte Carlo time. This could introduce a bias on this ensemble if the quantities we are studying are sensitive to topological charge. A study was made of this effect for decay constants in [70] and it was found that the impact of ‘topology freezing’ was 1% for f_K/f_π on set 8 and 1% for f_D . To allow for these effects, we therefore include an additional (correlated) uncertainty of 1% on all set 8 results in our final fit (this is already incorporated in test 0 of Fig. 4). We do this via a factor with prior 1.00(1), which returns a fit posterior of 0.993(5), showing that our set 8 results are consistent with those on our other sets.

Test 14 drops the data with physical m_l from the fit; in that case the fit uses the results with $m_l = m_s/5$ and $m_l = m_s$ to arrive at the physical light quark mass. This gives very similar central values but somewhat larger uncertainties. Test 16 instead drops the $m_l = m_s$ results; this has less impact on the uncertainties but shifts the central values at $q^2 = 0$ by about 1σ .

Test 17 looks at the inclusion of results from the spatial vector current as well as the temporal vector current. As expected from the discussion in Sec. II A, the use of the spatial vector current improves the vector form factor at large values of q^2 . Dropping these results, as in test 17,

increases uncertainties on the vector form factor value at q_{\max}^2 by a factor of 2.5. Figure 5 (top plot) shows the results for the form factor from spatial and temporal vector currents on sets 7 and 8 where we have both correlation functions (see Table XII in Appendix C). The plot shows the good agreement between the two sets of results and the considerably smaller uncertainties for the spatial vector current case, in agreement with what was seen in [38].

As discussed in Sec. II A, there is the possibility for $f_+^{V^0}$ and $f_+^{V^1}$ to differ by q^2 -dependent discretisation effects. To address this explicitly we plot the ratio $f_+^{V^1}/f_+^{V^0}$ against $(aq)^2$ in the lower plot of Fig. 5, taking into account the correlations between the two values from the fits. We see no evidence of discretisation effects at the $\sim 10\%$ level nor any q^2 trend in the results. We include terms in the fit to account for such effects for each ensemble and heavy mass,

$$f_+^{V^1}(q^2) = (1 + C^{a,m_h} \times (aq)^2) f_+^{V^0}(q^2), \quad (23)$$

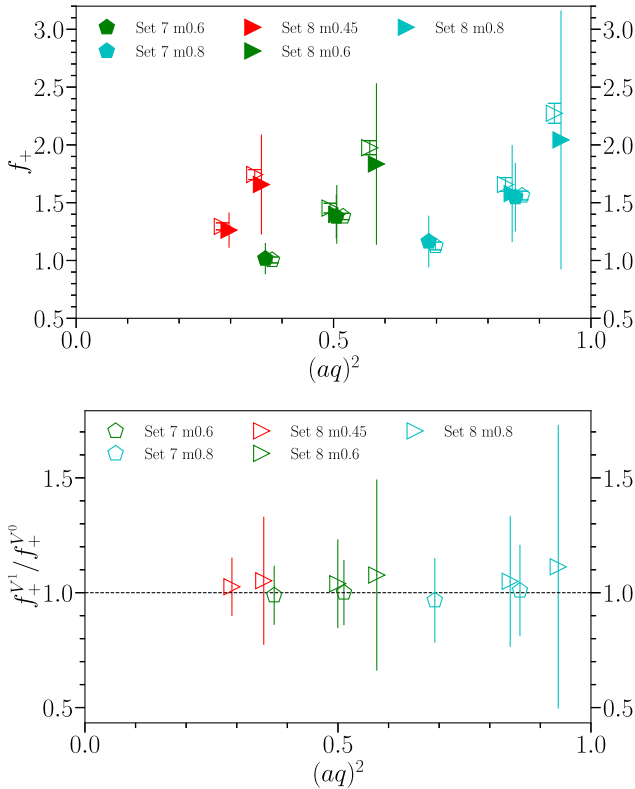


FIG. 5. Upper plot: A comparison of values and their statistical errors for the vector form factor derived from matrix elements for the spatial and temporal vector currents on ensembles where both are available. The filled symbols are the temporal vector results and the open symbols the spatial vector results. We have offset spatial vector results slightly on the q^2 -axis for clarity. Lower plot: The ratio of the f_+ values for the spatial and temporal vector cases. We see no evidence of any differences between them (within our uncertainties) that would indicate discretisation effects.

where the priors for all C s are 0.0(1). We find that our fits do not constrain these coefficients and including such terms makes no difference at all to the results of our fit, in keeping with Fig. 5. We include these terms in our final fit (test 0 of Fig. 4) nevertheless.

As noted above, we will quote our final form factors here at the physical value of m_l i.e. at the average of the physical u and d quark masses and in pure QCD (i.e. neglecting QED effects). The physical processes correspond either to a charged B meson decay with a u spectator quark, or a neutral B meson decay with a d spectator quark, however. As a test of isospin-breaking effects we can monitor the change in our results as we change the physical ratio of m_s/m_l [Eq. (18)] so that it matches that of m_s/m_u or m_s/m_d . To do this we take $m_d/m_u \approx 2$ [57]. We also switch to using the correct physical B and K masses, as opposed to using the average of the charged and neutral cases. We find that our form factors change by at most 0.5%, or 0.2σ . Note that this test is in fact an overestimate of strong isospin-breaking effects because it also changes the sea l masses to match either u or d which is not correct; the average of the light sea quark masses should remain m_l . No uncertainty is included in the form factors presented here to allow for QED effects or the isospin breaking effect discussed—both of these uncertainties will be addressed in the accompanying phenomenology paper.

IV. RESULTS

A. Evaluating form factors at the physical point

When it comes to evaluating form factors at the physical point and in the continuum limit, we simply need to take physical inputs for values in Eq. (11). Taking the valence and sea quark masses to their tuned values sets $\mathcal{N}_n^{0,+T} = 0$, and sending the lattice spacing $a \rightarrow 0$ means that, for any chosen M_H (in GeV),

$$a_n^{0,+T,(\text{cont})}(M_H) = \left(\frac{M_D^{\text{phys}}}{M_H}\right)^{\zeta_n} \left(1 + \rho_n^{0,+T} \log\left(\frac{M_H}{M_D^{\text{phys}}}\right)\right) \times \sum_{i=0}^{N_i-1} d_{i000n}^{0,+T} \left(\frac{\Lambda_{\text{QCD}}}{M_H}\right)^i, \quad (24)$$

where $\Lambda_{\text{QCD}} = 0.5$ GeV as usual. These are the values for a_n which are given in Tables V and VIII for $M_H = M_B^{\text{phys}}$ and $M_H = M_D^{\text{phys}}$ respectively. As already discussed, our results are for $m_u = m_d = m_l$ so we use the average of the charged and neutral B, K and D masses from [57] when required. These masses can be used in Eq. (12) to obtain z from any given q^2 and M_H . Finally, $\mathcal{L}^{\text{cont}}(M_H)$ [Eq. (15)] is evaluated using $x_\pi^{\text{phys}}, x_K^{\text{phys}}, x_\eta^{\text{phys}}, \delta_{FV} = 0$ and evaluating g [Eq. (17)] at M_H . The resulting $\mathcal{L}(M_H)$ values at $M_H = M_B^{\text{phys}}$ and $M_H = M_D^{\text{phys}}$ are also given in Tables V and VIII.

TABLE V. Values of fit coefficients $a_n^{0,+T}$, pole masses, and the \mathcal{L} term with correlation matrix below, evaluated at the physical point and the B mass. Note that $a_0^+ = a_0^0$. Masses are in GeV. The pole masses and \mathcal{L} are very slightly correlated due to the way the fit function is constructed. These correlations are too small to have any meaningful effect on the fit, but we include them for completeness. See Appendix A for details of reconstructing our results.

$a_0^{0/+}$	a_1^0	a_2^0	a_1^+	a_2^+	a_0^T	a_1^T	a_2^T	$M_{B_{s0}}^{\text{phys}}$	$M_{B_s^*}^{\text{phys}}$	\mathcal{L}
0.2545(90)	0.210(76)	0.02(17)	-0.71(14)	0.32(59)	0.255(18)	-0.66(23)	0.36(84)	5.729495(85)	5.4158(15)	1.304(10)
1.00000	0.80619	0.56441	0.30543	0.04776	0.42939	0.19136	0.06240	-0.00032	-0.00197	-0.19815
	1.00000	0.91180	0.35256	0.06186	0.31091	0.16899	0.05677	0.00006	-0.00250	0.02839
		1.00000	0.28531	0.08655	0.18297	0.09938	0.04827	0.00005	-0.00181	0.03245
			1.00000	0.84649	0.06813	0.09633	0.05829	0.00074	-0.01316	0.09126
				1.00000	-0.02470	0.02366	0.04442	-0.00054	0.00963	0.00353
					1.00000	0.59841	0.32316	-0.00030	0.00167	-0.11487
						1.00000	0.85349	0.00032	-0.00574	0.04788
							1.00000	-0.00046	0.00825	0.00184
								1.00000	0.00003	-0.00003
									1.00000	0.00052
										1.00000

Putting all of this together,

$$\begin{aligned}
 f_0^{\text{cont}}(q^2, M_H) &= \frac{\mathcal{L}^{\text{cont}}(M_H)}{1 - \frac{q^2}{M_{H_{s0}}^*}} \sum_{n=0}^{N-1} a_n^{0,(\text{cont})}(M_H) z^n \\
 f_+^{\text{cont}}(q^2, M_H) &= \frac{\mathcal{L}^{\text{cont}}(M_H)}{1 - \frac{q^2}{M_{H_s^*}^*}} \sum_{n=0}^{N-1} a_n^{+,(\text{cont})}(M_H) \\
 &\quad \times \left(z^n - \frac{n}{N} (-1)^{n-N} z^N \right) \\
 f_T^{\text{cont}}(q^2, M_H) &= \frac{\mathcal{L}^{\text{cont}}(M_H)}{1 - \frac{q^2}{M_{H_s^*}^*}} \sum_{n=0}^{N-1} a_n^{T,(\text{cont})}(M_H) \\
 &\quad \times \left(z^n - \frac{n}{N} (-1)^{n-N} z^N \right), \quad (25)
 \end{aligned}$$

where the two pole masses are evaluated using $M_{H_{s0}}^* = M_H + \Delta$ and Eq. (13) as usual, working in GeV and not lattice units. These pole masses are also given in Tables V and VIII. We have used the superscript ‘cont.’ here to emphasise that these expressions are valid in the continuum (with tuned quark masses) only, but we drop this superscript in the results tables and numerical results which follow, noting that all results are presented in this limit. For details on loading our results from the supplied python script, see Appendix A.

B. $B \rightarrow K$ form factor results

Figures 6, 7, and 8 show our lattice results and fit functions in z space. The points plotted correspond to $(1 - q^2/M^2)f$ where $(1 - q^2/M^2)$ is the pole factor on the right-hand side of Eq. (11) for each form factor. The figures show results on each ensemble for each value of am_h ,

joined by the line from the fit corresponding to those parameters. The final result in the continuum, at the B mass and physical quark masses is shown by the solid band. We see that the lattice results lie on approximately linear curves in all cases. This is particularly clear for the scalar form factor case in Fig. 6. This makes for a benign z expansion and justifies our choice of $N = 3$, as is also confirmed by the $\log(\text{GBF})$ value. Dark blue data points correspond to the charm quark mass on each ensemble. We can see here that, at this mass, discretization effects are small with very good agreement between data on different ensembles, particularly in the scalar and vector cases. Otherwise we can see data points arranged according to mass, moving towards the b mass, which is close to the $am_h = 0.8$ value on our finest ensemble, set 8. This is shown from the proximity of set 8 data to the physical band in the plots. We see that the twist choices on our finest ensemble also give good coverage of the full z range (shown by the physical band curves) at the physical point.

We present our final scalar, vector and tensor form factors evaluated at the physical B mass, physical quark masses, and in the continuum limit, across the full range of physical q^2 values in Fig. 9. The similarity of f_+ and $f_T(\mu = 4.8 \text{ GeV})$ is very obvious, an assumption that was often used to estimate f_T from f_+ before reliable f_T calculations existed.

A breakdown of the percentage error contributions to each form factor across the q^2 range is given in Fig. 10. The largest contribution in all cases is from statistics, followed by the expansion in the heavy mass. All other errors, from quark mistuning (including the chiral logs \mathcal{L} and analytic chiral terms), discretization effects and input masses are small. As noted above, the contribution of the heavy-mass expansion to the error is also apparent in Fig. 4.

Further error analysis is displayed in Fig. 11, which gives a breakdown of the contributions of each of the ensembles

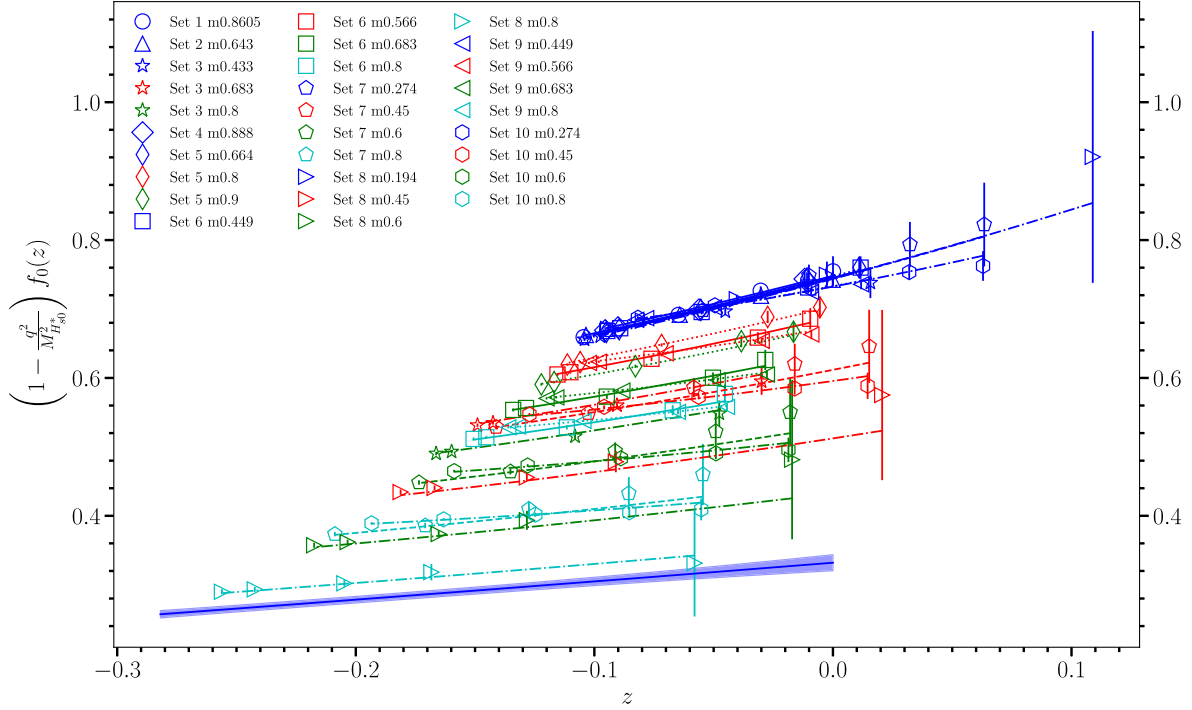


FIG. 6. $\left(1 - \frac{q^2}{M_{H_s}^2}\right) f_0(z)$ data points and final result at the physical point (blue band). Data points are labelled by heavy quark mass, where e.g. m0.8 indicates $am_h = 0.8$ on that ensemble. Lines between data points of a given heavy mass are the result of the fit evaluated on this ensemble and mass with all lattice artefacts present. Sets 9 and 10 are the $H_s \rightarrow \eta_s$ data from sets 1 and 2 in [32], which were fitted simultaneously with sets 6 and 7 respectively.

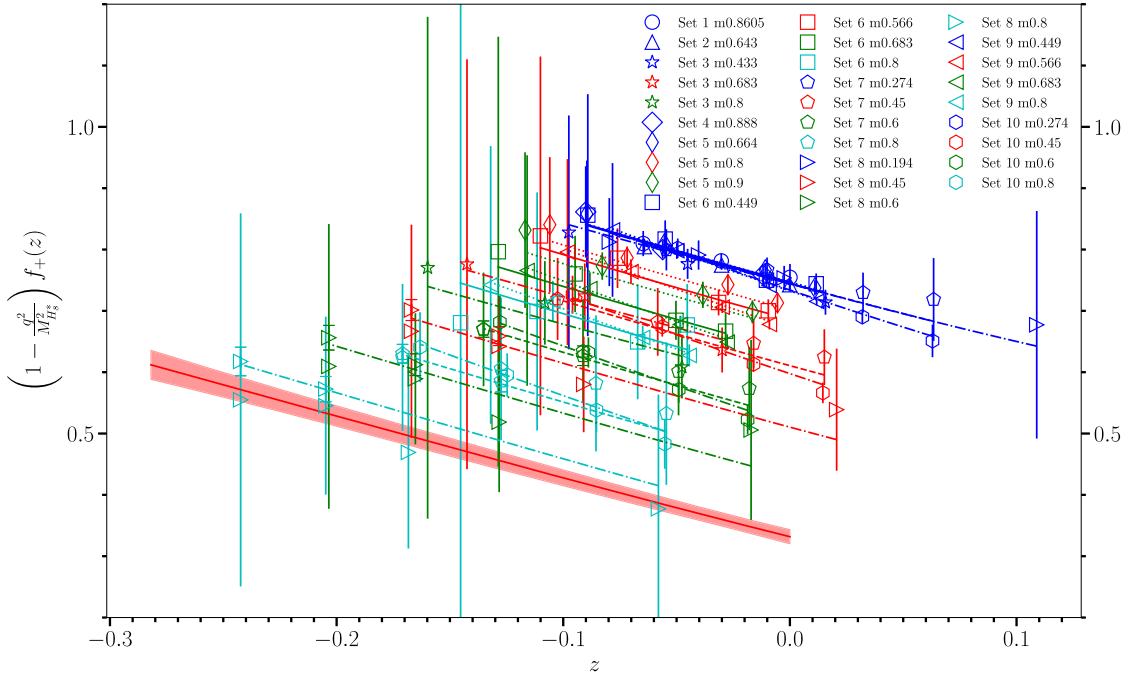


FIG. 7. $\left(1 - \frac{q^2}{M_{H_s}^2}\right) f_+(z)$ data points and final result at the physical point (red band). Data points are labelled by heavy quark mass, where e.g. m0.8 indicates $am_h = 0.8$ on that ensemble. Lines between data points of a given heavy mass are the result of the fit evaluated on this ensemble and mass with all lattice artefacts present. Sets 9 and 10 are the $H_s \rightarrow \eta_s$ data from sets 1 and 2 in [32], which were fitted simultaneously with sets 6 and 7 respectively. At large $|z|$ (large q^2), data obtained from both temporal and spatial components of V^μ are shown, the latter with end caps specifying the associated uncertainty. As discussed in Sec. II, errors for f_+ at large q^2 are significantly smaller when obtained from spatial vector components.

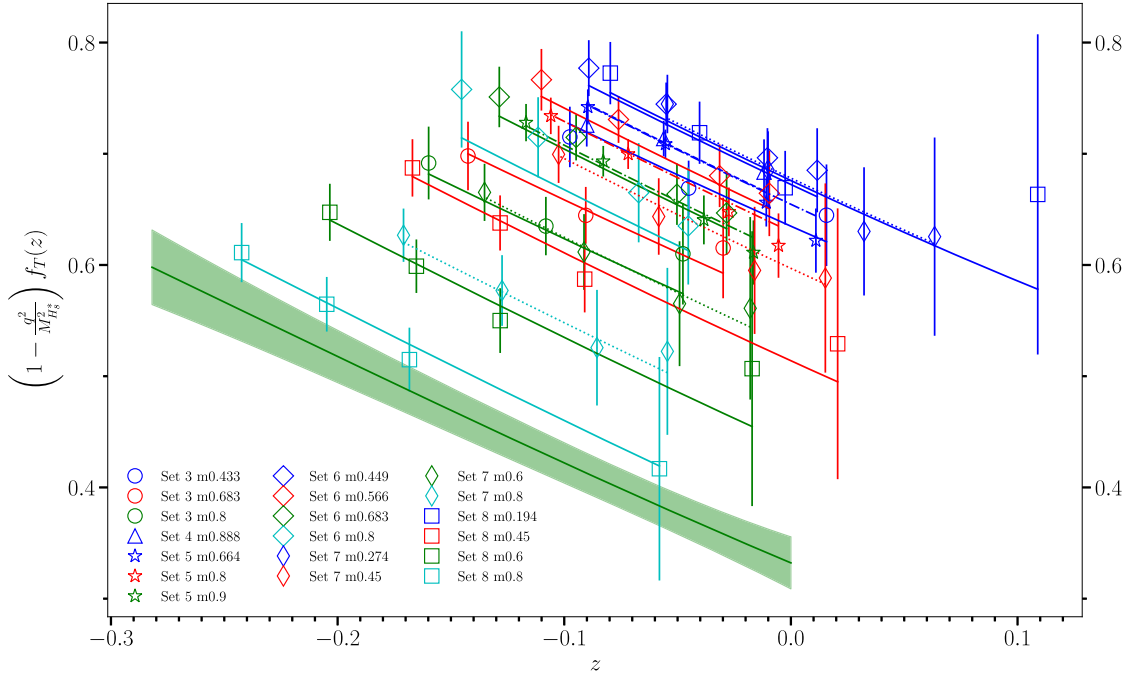


FIG. 8. $\left(1 - \frac{q^2}{M_H^2}\right) f_T(z)$ data points and final result at the physical point (green band). Data points are labelled by heavy quark mass, where e.g. m0.8 indicates $am_h = 0.8$ on that ensemble. Lines between data points of a given heavy mass are the result of the fit evaluated on this ensemble and mass with all lattice artefacts present.

listed in Table I to the statistical uncertainty of each form factor at its extremal values of q^2 . The contributions are normalized to a total variance of 1 in each case, and we note that sets 6 and 7 include contributions from the additional $H_s \rightarrow \eta_s$ data on those ensembles. We see that sets 7 and 8 make the largest contributions to the uncertainties of all form factors across the q^2 range, with set 1 making the smallest contribution in all cases. This error could be reduced with better statistics on the superfine and ultrafine ensembles (sets 7 and 8), perhaps also including an additional heavier mass at $am_h = 0.9$ on set 8, or with a further, even finer ensemble, at the bottom mass. This would be a

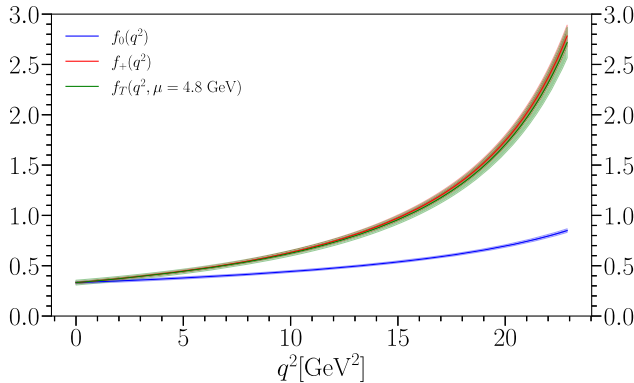


FIG. 9. Final $B \rightarrow K$ form factor results at the physical point across the full q^2 range.

numerically expensive, but straightforward, exercise to reduce uncertainty in future.

1. Results at q_{\max}^2

In order to test the ability of our fit to handle M_H dependence independently of q^2 dependence we perform a simpler fit in M_H at a fixed q^2 point for comparison to our full fit. For this we use our values for f_0 at q_{\max}^2 (only) and fit them to the functional form:

$$f_0^{M_H \text{ fit}}(q_{\max}^2) = \frac{\mathcal{L}}{1 - \frac{q_{\max}^2}{M_{H^*}^2}} \left(1 + \rho_0^0 \log\left(\frac{M_H}{M_D}\right)\right) \times (1 + \mathcal{N}_0^0) \times \sum_{i,j,k,l=0}^{N_{ijkl}-1} d_{ijkl}^0 \left(\frac{\Lambda_{\text{QCD}}}{M_H}\right)^i \left(\frac{am_h^{\text{val}}}{\pi}\right)^{2j} \times \left(\frac{a\Lambda_{\text{QCD}}}{\pi}\right)^{2k} (x_\pi - x_\pi^{\text{phys}})^l, \quad (26)$$

taking the same choices for N_{ijkl} and priors as for our full fit using Eqs. (11) and (14). Figure 12 shows the $f_0(q_{\max}^2)$ data on each ensemble, as well as the result of our standard “full” fit to all data and the fit of the $f_0(q_{\max}^2)$ alone [Eq. (26)].

Since Fig. 12 is a plot of results and a fit that depend only on M_H , it is easier to see here that we have good coverage of M_H values from M_D to M_B . The dashed lines connecting

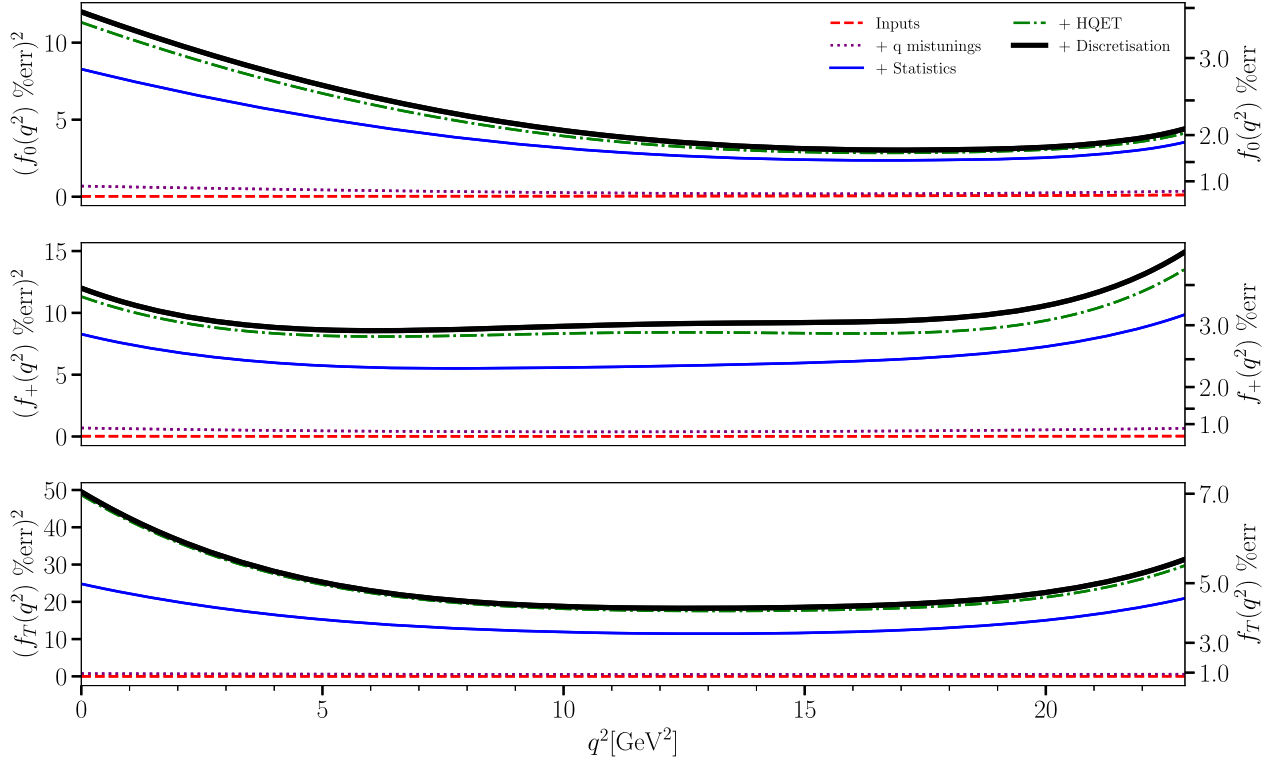


FIG. 10. The contributions to the total percentage error (black line) of $B \rightarrow K$ form factors $f_0(q^2)$ (top) and $f_+(q^2)$ (middle) and $f_T(q^2)$ (bottom) from different sources, shown as an accumulating error. The red dashed line (‘inputs’) includes values for parameters, such as masses, taken from the particle data group (PDG) [57] and used in the fit as described above. The purple dotted line (“ q mistunings”) adds, negligibly, to the inputs of the error contribution from the quark mistunings associated with c fit parameters and errors from the light-quark chiral extrapolation, while the solid blue line (“statistics”) further adds the error from our correlator fits. The green dotted-dashed line (“HQET”) includes the contribution from the expansion in the heavy-quark mass, and, finally, the thick black line (“Discretization”), the total error on the form factor, also includes the discretization errors. In the case of the tensor form factor, the difference here is so small as to obscure the HQET line. The percentage variance adds linearly and the scale for this is given on the left-hand axis. The percentage standard deviation, the square root of this, can be read from the scale on the right-hand side.

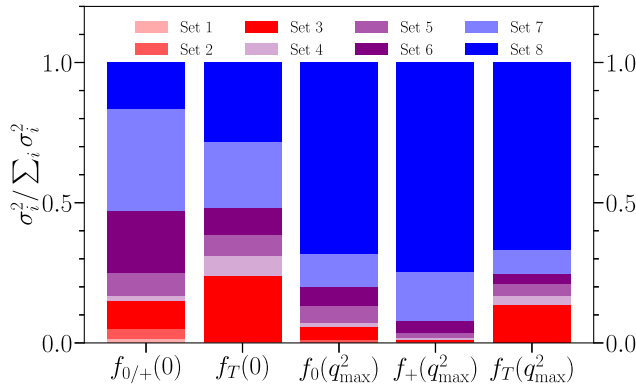


FIG. 11. Breakdown of the contributions to the statistical uncertainty of the $B \rightarrow K$ form factors at their extremes from data on each ensemble. Uncertainty from each ensemble σ_i is added in quadrature, normalized by the total uncertainty squared $\sum_i \sigma_i^2$. Sets 6 and 7 include contributions from $H_s \rightarrow \eta_s$ data.

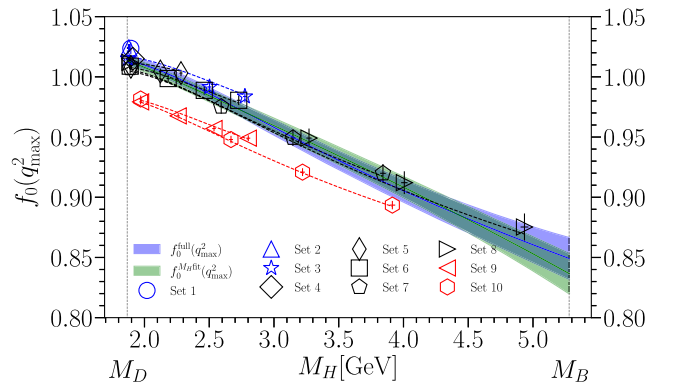


FIG. 12. The $f_0(q_{\max}^2)$ data points on each ensemble, plotted against M_H . Points in blue have physical m_l values, black have $m_l = m_s/5$ and red have $m_l = m_s$. The blue band indicates the continuum result from our full fit [i.e. Eq. (25)]. The green band indicates the continuum results of a fit of just the $f_0(q_{\max}^2)$ data to Eq. (26). Dashed lines between data points indicate the full fit evaluated at that lattice spacing.

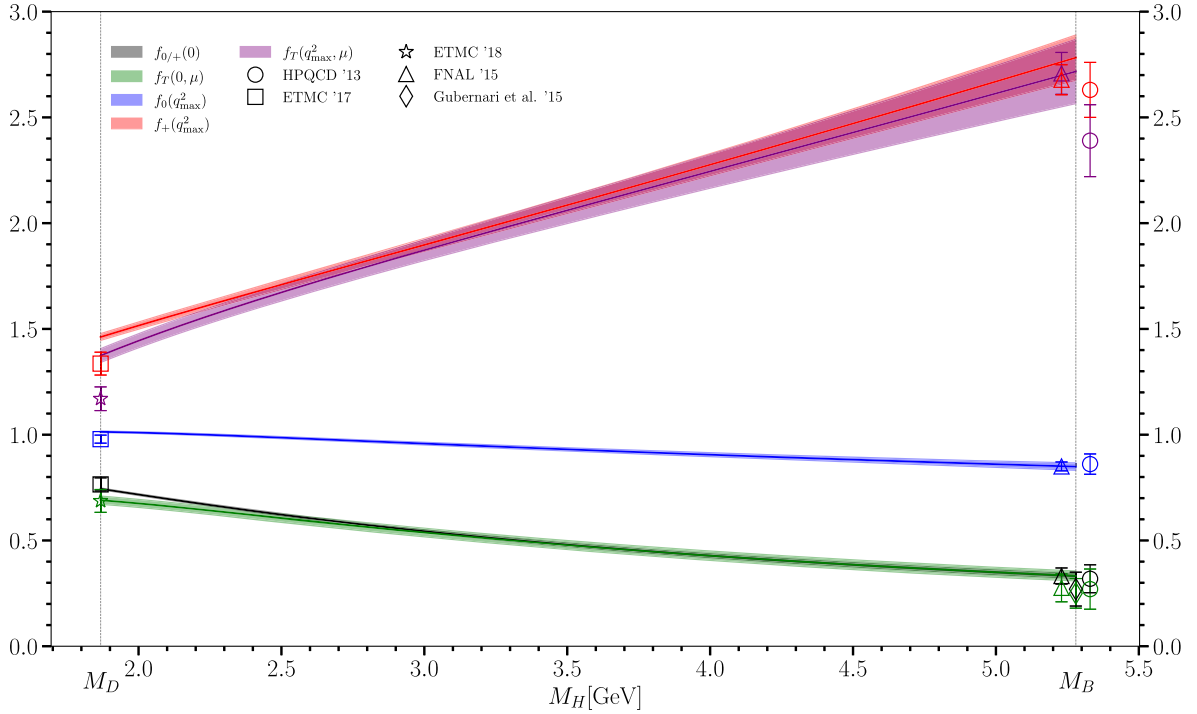


FIG. 13. The form factors at q_{\max}^2 and $q^2 = 0$ evaluated across the range of physical heavy masses from the D to the B . Other lattice studies [25,28,71,72] of both $D \rightarrow K$ and $B \rightarrow K$ are shown for comparison. We also include some $B \rightarrow K$ results at $q^2 = 0$ from Gubernari *et al.* [73], a calculation using light-cone sum rules. We do not include HPQCD's $D \rightarrow K$ results that share data with our calculation here [36]; see text for a discussion of that comparison. At the B end, data points are offset from M_B for clarity. Note that we have run Z_T to scale μ in this plot, where μ is defined linearly between 2 GeV and $m_b = 4.8$ GeV, according to Eq. (27). The full running to 2 GeV from m_b results in a factor of 1.0773(17), applied to $f_T^{D \rightarrow K}$.

results at a fixed lattice spacing make clear how the discretization effects behave, peeling away from the continuum curve for larger am_h values. Our range of am_h values (see Sec. II C) allows our fit to track the discretization effects. The smaller fit $f_0^{M_H \text{fit}}(q_{\max}^2)$ agrees well with our full fit result, indicating that we do indeed have good control of both q^2 and M_H dependence in our fit. We repeat this test with versions of Eq. (26) which include $(M_D/M_H)^{\zeta_0}$ terms, where we trial $\mathcal{P}[\zeta_0] = 1.5(0.5)$ and $\mathcal{P}[\zeta_0] = -0.5(0.5)$. In both cases, the fit agrees within 1σ with our full fit and the fit of Eq. (26). Indeed, we find that the fit output hardly changes when we fix the power ζ_0 in Eq. (26) to be exactly 1.5, showing that the output is determined by the lattice results and is not constrained by the presence or absence of the initial power term.

C. Connecting $B \rightarrow K$ and $D \rightarrow K$ form factors

Our heavy-HISQ approach allows us to study in detail the behavior of the form factors at fixed q^2 with a change in heavy-quark mass from the c to the b . Figure 13 illustrates this smooth variation with a plot of the continuum form factors, at extremal q^2 values, plotted against heavy-mass M_H from M_D^{phys} to M_B^{phys} . This allows us to compare with previous calculations, both for $B \rightarrow K$ and $D \rightarrow K$, which

we will discuss below. Firstly, however, we take a moment to address the running normalization of $f_T(q^2, \mu)$.

In our calculation of the tensor form factor, we used $Z_T(\mu = 4.8 \text{ GeV})$, calculated in [42]. The scale μ is taken to be approximately equal to m_b^{pole} . While this is appropriate for the $B \rightarrow K$ results, we use a smaller scale, $\mu = 2 \text{ GeV}$, for $D \rightarrow K$ to compare to previous results. In order to produce results at arbitrary M_H , we use a linear interpolation of μ between these two values,

$$\mu(M_H)[\text{GeV}] = 2 + \frac{2.8}{M_B^{\text{phys}} - M_D^{\text{phys}}} (M_H - M_D^{\text{phys}}). \quad (27)$$

Following [42], we then run from $\mu(M_B) = 4.8 \text{ GeV}$ to our desired μ scale. The maximal extent of this running is down to 2 GeV (i.e. for $M_H = M_D$), and this results in a factor of 1.0773(17) multiplying $f_T(q^2, 4.8 \text{ GeV})$.

Returning to Fig. 13 and focusing on the $B \rightarrow K$ end of the results, we see very good agreement with previous work in general, adding confidence in the heavy-HISQ method. We find improvements in precision across the form factors, particularly at $q^2 = 0$, which is the important region for comparison to experiment in this case. At q_{\max}^2 our precision is not as high as that achieved in

TABLE VI. Form factor results at the q^2 extremes. As described in the text, the $f_0^{D \rightarrow K}$ and $f_+^{D \rightarrow K}$ share data with the results in [36] (included for comparison) so should not be viewed as an independent calculation.

	$q^2 = 0$	$q^2 = q_{\max}^2$
	This work	
$f_0^{B \rightarrow K}(q^2)$	0.332(12)	0.849(17)
$f_+^{B \rightarrow K}(q^2)$	0.332(12)	2.78(11)
$f_T^{B \rightarrow K}(q^2, \mu = 4.8 \text{ GeV})$	0.332(24)	2.72(15)
$f_0^{D \rightarrow K}(q^2)$	0.7441(40)	1.0136(36)
$f_+^{D \rightarrow K}(q^2)$	0.7441(40)	1.462(16)
$f_T^{D \rightarrow K}(q^2, \mu = 2 \text{ GeV})$	0.690(20)	1.374(33)
	c.f. $D \rightarrow K$ [36]	
$f_0^{D \rightarrow K}(q^2)$	0.7380(44)	1.0158(41)
$f_+^{D \rightarrow K}(q^2)$	0.7380(44)	1.465(20)

[28]. Our results have not been optimized for the q_{\max}^2 region, however, so improvement there is readily possible. We also have the advantage that our renormalization constants are more accurately calculated, which can otherwise be a source of systematic uncertainty. In [28], one-loop perturbation theory is used to determine the current renormalization factors and estimates made of the impact of missing α_s^2 terms in these factors. Table VI provides numerical values for our $B \rightarrow K$ (as well as $D \rightarrow K$; see Sec. IV E) form factors at the q^2 extremes shown in Fig. 13.

Figure 13 shows that the form factors at $q^2 = 0$ as well as $f_0(q_{\max}^2)$ fall slowly as M_H is increased. In contrast f_+ and f_T at q_{\max}^2 increase. We can isolate the effective leading power of M_H dependence by determining $X^{\text{eff}} = M_H/f \times df/dM_H$, which returns X for $f \propto M_H^X$. Our results for the form factors at $q^2 = 0$ and q_{\max}^2 are plotted in Fig. 14. We see that at q_{\max}^2 for $M_H \rightarrow M_B$, the dependence is $X^{\text{eff}} \approx -0.3$ for f_0 , and $X^{\text{eff}} \approx +0.7$ for $f_{+/T}$. This is roughly consistent with the values of -0.5 and $+0.5$ predicted in the

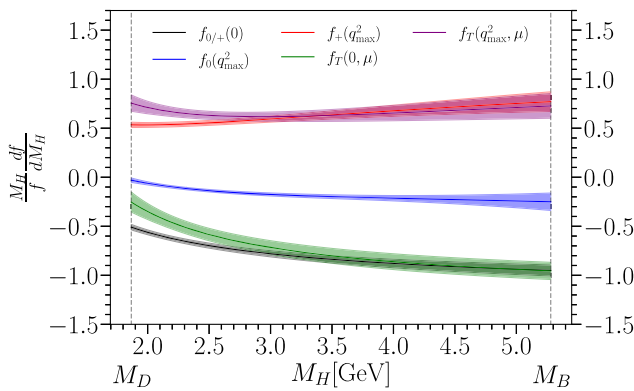


FIG. 14. The leading power of M_H dependence in the form factors at $q^2 = 0$ and q_{\max}^2 . The scale associated with the tensor form factor, μ , is varied using Eq. (27).

infinite mass limit by HQET [69]. It is clear that our fit is flexible enough to allow for M_H dependence to vary with q^2 . This flexibility arises from the fact that we are fitting in z space with independent coefficients for different powers of z [see Eq. (14)]. Our lattice QCD results then have sufficient coverage of z/q^2 and M_H space (in the range of masses from M_D up to $0.9M_B$) to give a robust fit result at M_B across the full kinematic range. The effective powers of M_H that we obtain at the two ends of the range, $q^2 = 0$ and q_{\max}^2 , when $M_H = M_B$ provide a test of HQET. Note that Fig. 14 is essentially unchanged under the different fit possibilities that we test in Fig. 4 for the $(M_D/M_H)^\zeta$ terms in our fit. Thus the effective powers of M_H that we obtain at M_B are not dependent on the details of the fit form that we use, including how much input from HQET we impose.

A similar plot is presented in Appendix B (Fig. 22), for fixed $q^2 = M_D^2$.

1. HQET tests of $B \rightarrow K$ results

Returning to our $B \rightarrow K$ form factors, HQET expectations [Ref. [69], Eqs. (19) and (20)] give relations

$$\frac{M_B}{M_B + M_K} = (f_+(E_K) - f_0(E_K)) \frac{M_B^2}{q^2 f_T(E_K)}, \quad (28)$$

$$\frac{M_B}{M_B + M_K} = \left(\left(1 - \frac{E_K}{M_B} \right) f_+(E_K) - \frac{f_0(E_K)}{2} \right) \frac{M_B^2}{q^2 f_T(E_K)}. \quad (29)$$

Both Eqs. (28) and (29) are expected to be valid at small recoil (i.e. for $E_K \rightarrow M_K \approx 0.5$ GeV), while only Eq. (28) [Ref. [69], Eq. (19)] should be valid for large recoil. Figure 15 plots the form factor combinations (using $f_T(\mu = 4.8 \text{ GeV})$) as a function of E_K . It shows the expected constant value of the form factor combination

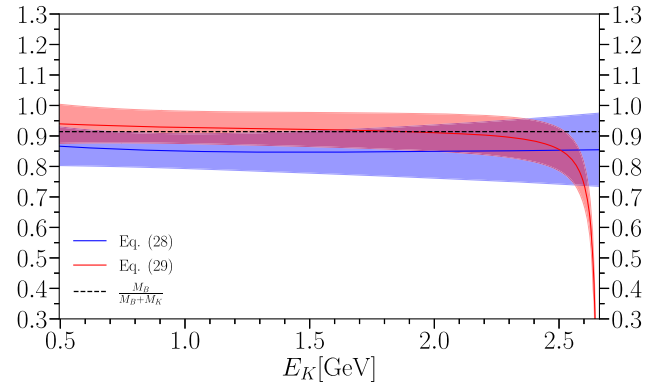


FIG. 15. Combinations of $B \rightarrow K$ form factors, f_0 , f_+ and $f_T(\mu = 4.8 \text{ GeV})$ in Eqs. (28) and (29) compared with expectations $\frac{M_B}{M_B + M_K}$ from HQET [69] (dashed line). Uncertainties on the HQET expectations are not included.

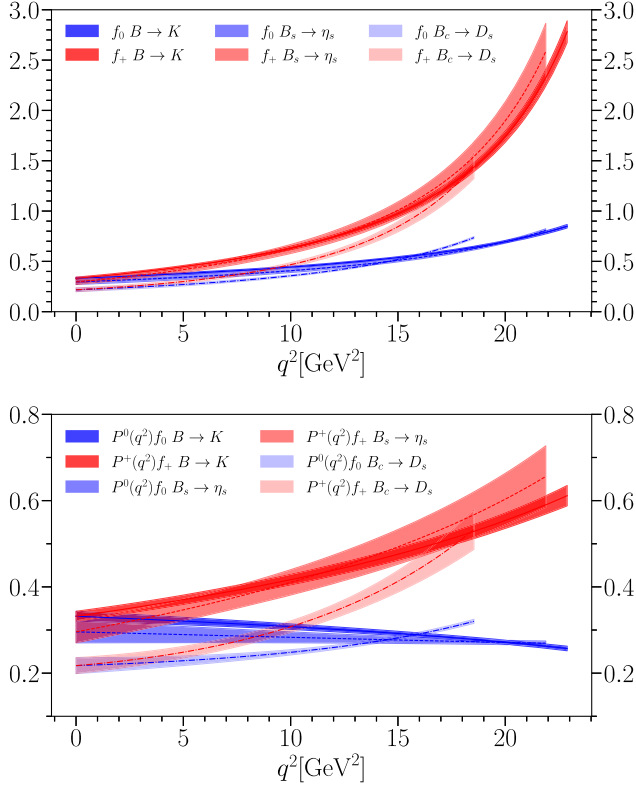


FIG. 16. Comparison of our $B \rightarrow K$ scalar and vector form factors with those of $B_s \rightarrow \eta_s$ [32] and $B_c \rightarrow D_s$ [38] to show the impact of changing the spectator quark mass. In the lower panel, we have multiplied the form factors by their common pole factors to reduce the y-axis range and highlight the variation between the form factors. We take $P^0(q^2) = 1 - \frac{q^2}{M_{B_s^0}^2}$, $P^+(q^2) = 1 - \frac{q^2}{M_{B_s^*}^2}$, using the central values of the masses in Table V.

of Eq. (28) across the full q^2 range. It also shows the failure of Eq. (29) at large recoil (large E_K).

D. Connecting $B \rightarrow K$ to other form factors

Figures 16 and 17 show the effect of changing spectator quark mass on the $b \rightarrow s$ pseudoscalar meson to pseudoscalar meson form factors. We compare our $B \rightarrow K$ results to the $B_s \rightarrow \eta_s$ results in [32], which differ only in the light spectator quark becoming a strange quark, and $B_c \rightarrow D_s$ results [38], where the spectator is a heavy (charm) quark. We see very mild spectator quark dependence for the light/strange quarks, at most a deviation of $\approx 1\sigma$, which is roughly consistent with the modest effect of setting $\mathcal{L} = 1$ in Fig. 4. The transition to a heavy c spectator leads to a much larger change. The heavier spectator gives a smaller form factor at $q^2 = 0$ that rises more steeply to q_{\max}^2 , which has a smaller value. The behavior of f_T shown in Fig. 17 is similar, but with a smaller shift at $q^2 = 0$.

We can also conduct a test of our chiral extrapolation by comparison with the $B_s \rightarrow \eta_s$ in [32]. By setting

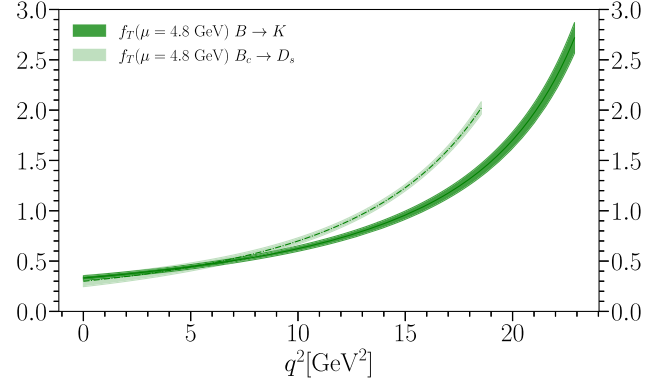


FIG. 17. Comparison of our $B \rightarrow K$ tensor form factor (at $\mu = 4.8$ GeV) with those of $B_c \rightarrow D_s$ [38] to show the impact of changing the spectator quark mass.

$m_l/m_s = 1$, $M_B^{\text{phys}} \rightarrow M_{B_s}^{\text{phys}}$, $M_D^{\text{phys}} \rightarrow M_{D_s}^{\text{phys}}$, and $M_K^{\text{phys}} \rightarrow M_{\eta_s}^{\text{phys}}$ in our evaluation of Eq. (25), we can obtain results for $B_s \rightarrow \eta_s$. These are not completely independent of the results in [32] as they include shared data on two sets (see Sec. II C). However, the correlator and z -expansion fits used here and in that work are very different, and we do not include data on set 8 (set 3 in [32]), nor the continuum $f_0(q_{\max}^2)$ data point that was added there. This makes comparison of our results a strong test of our fit, particularly the chiral perturbation theory element. Table VII gives the results of our form factors evaluated at $B_s \rightarrow \eta_s$, at extremal q^2 values. We see that they are in good agreement with the results in [32], supporting our extrapolation in the spectator mass. Additionally, we note that they agree very well with the $f_0(q_{\max}^2)$ value given in [74]. This point was included in the analysis in [32], and here we demonstrate that we are able to obtain a very similar result independently of this point.

TABLE VII. A comparison of form factor results for $B_s \rightarrow \eta_s$ at the q^2 extremes, obtained here and in earlier work. As described in the text, the f_0 and f_+ obtained here share data with the results in [32] (included for comparison) so should not be viewed as an independent calculation.

	$q^2 = 0$	$q^2 = q_{\max}^2$
	This work	
$f_0^{B_s \rightarrow \eta_s}(q^2)$	0.3191(85)	0.819(17)
$f_+^{B_s \rightarrow \eta_s}(q^2)$	0.3191(85)	2.45(19)
$f_T^{B_s \rightarrow \eta_s}(q^2, \mu = 4.8 \text{ GeV})$	0.370(78)	2.32(56)
	c.f. $B_s \rightarrow \eta_s$ [32]	
$f_0^{B_s \rightarrow \eta_s}(q^2)$	0.296(25)	0.808(15)
$f_+^{B_s \rightarrow \eta_s}(q^2)$	0.296(25)	2.58(28)
	c.f. $B_s \rightarrow \eta_s$ [74]	
$f_0^{B_s \rightarrow \eta_s}(q^2)$...	0.811(17)

E. $D \rightarrow K$ form factors

By evaluating our form factors at the D mass, we are able to calculate scalar, vector and tensor form factors for the $D \rightarrow K$ decay. The scalar and vector form factors are in agreement with those in [36] (see Table VI for a comparison). While these two calculations share a considerable amount of raw correlator data, these data (except for sets 1 and 2) are subject to very different and much larger correlator fits here, involving more masses as well as tensor three-point data, and the accompanying non-Goldstone kaons. As well as these different correlator fits, our heavy-HISQ method uses a very different modified z expansion from that in [36], in order to include heavy-mass dependence. That we see agreement here, with a maximal difference of 1σ (assuming correlations are modest), indicates that our uncertainties are of an appropriate size.

Our fit coefficients for the $D \rightarrow K$ form factors, along with their correlations, are given in Table VIII. Our form factors can be reconstructed from these values, or the PYTHON script described in Appendix A can be used. As discussed above, we run the scale of Z_T down to 2 GeV for the $D \rightarrow K$ results, as used in [72]. Following [42] this involves multiplying by 1.0773(17), a factor which is included in the a_n^T values in Table VIII and in our results quoted in Table VI. Note that this is the same value used at the M_D end of results in Fig. 13.

Returning to the $D \rightarrow K$ end of the results in Fig. 13, we again see good agreement with previous work, with the exception of $f_T(q_{\max}^2, 2 \text{ GeV})$ and $f_+(q_{\max}^2)$ where we are in tension with ETMC [71,72]. This was found previously for $f_+(q_{\max}^2)$ in [36].

Our tensor form factor is compared to that from [72] in Fig. 18. We see that the uncertainty is reduced by roughly a factor of 2 across the q^2 range in our results. Good agreement is seen with [72] at low q^2 . Additionally,

TABLE VIII. $D \rightarrow K$ values of fit coefficients a_n^T , the pole mass in GeV, and the \mathcal{L} term with correlation matrix below (see Eq. (25) for fit form). The pole mass and \mathcal{L} are very slightly correlated due to the way the fit function is constructed. These correlations are too small to have any meaningful effect on the form factor values, but we include them for completeness. For details on reconstructing our results, see Appendix A. a_n^T values include a factor of 1.0773(17) from running Z_T to $\mu = 2 \text{ GeV}$.

a_0^T	a_1^T	a_2^T	$M_{D_s^*}^{\text{phys}}$	\mathcal{L}
0.522(15)	-0.74(13)	0.38(84)	2.11220(40)	1.3234(24)
1.00000	0.34687	0.03704	-0.00005	-0.06075
	1.00000	0.61200	-0.01018	0.01148
		1.00000	0.00069	-0.00046
			1.00000	0.00003
				1.00000

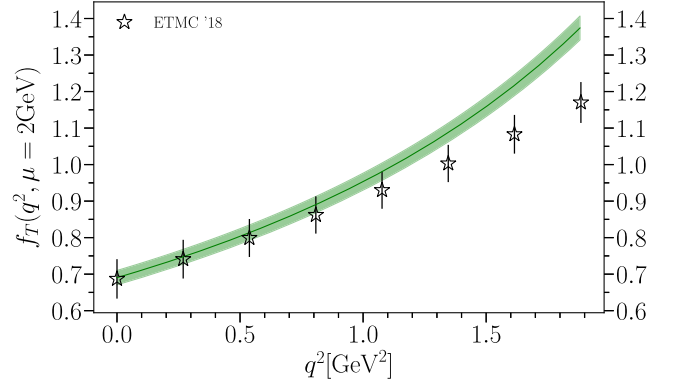


FIG. 18. The green band gives our $D \rightarrow K$ tensor form factor at $\mu = 2 \text{ GeV}$, across the physical q^2 range. Results from [72] are included for comparison.

we report the ratio $f_T^{D \rightarrow K}(0, \mu = 2 \text{ GeV})/f_+^{D \rightarrow K}(0) = 0.928(27)$, which agrees with the 0.898(50) given in [72]. However, our tensor form factor has a steeper slope in q^2 and at q_{\max}^2 there is disagreement at a level of 3.1σ .

Figure 19 gives the breakdown of statistical uncertainty from each ensemble for the $D \rightarrow K$ form factors. It is clear from Fig. 19 that, unlike in the $B \rightarrow K$ case above (Fig. 11), the errors on all $D \rightarrow K$ form factors across the q^2 range are dominated by the coarser lattices, specifically the physical sets 2 and 3, while again set 1 makes the smallest contribution in all cases except $f_+(q_{\max}^2)$. This makes sense, as the physical charm mass is easily accessed on all ensembles, so the heavy-quark extrapolation does not play much of a role here. The extrapolation to physical light-quark mass is relatively more important, so sets 1, 2 and 3 play a bigger role. Sets 1 and 2 do not contain any tensor data; hence, set 3 is especially dominant in the case of f_T .

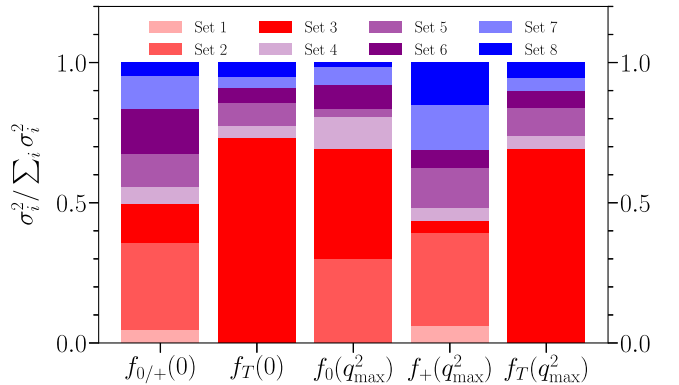


FIG. 19. Breakdown of the contributions to the statistical uncertainty of the $D \rightarrow K$ form factors at their extremes from data on each ensemble. Uncertainty from each ensemble σ_i is added in quadrature, normalized by the total uncertainty squared $\sum_i \sigma_i^2$. Sets 6 and 7 include contributions from $H_s \rightarrow \eta_s$ data.

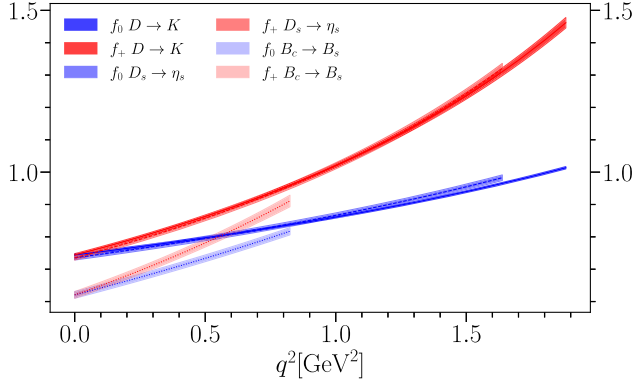


FIG. 20. Comparison of our $D \rightarrow K$ scalar and vector form factors with those for $D_s \rightarrow \eta_s$ [32] and $B_c \rightarrow B_s$ [34] to show the effect of changing spectator quark mass.

F. Connecting $D \rightarrow K$ to other form factors

As with $b \rightarrow s$ decays above, we now have sufficient information from accurate lattice QCD calculations to test the impact on the pseudoscalar-to-pseudoscalar meson form factors of changing the quark mass for the spectator quark that accompanies the $c \rightarrow s$ decay. Figure 20 shows this effect. We compare our $D \rightarrow K$ results to the $D_s \rightarrow \eta_s$ results from [32] and, as for $b \rightarrow s$, see a very gentle dependence when we change the spectator from light to strange. This agrees with the conclusions of [41] but is much more compelling here because of the high precision of both sets of form factors. The biggest deviation is for f_0 , at the maximum q^2 for $D_s \rightarrow \eta_s$, where $D_s \rightarrow \eta_s$ is larger than $D \rightarrow K$ by $\approx 2\sigma$ (or about 2%).

We can also compare with $B_c \rightarrow B_s$ form factors [34], where the spectator quark is a b quark. This is a very big change in spectator quark mass (roughly a factor of 1000) and unsurprisingly we see a much bigger change. The form factors for $B_c \rightarrow B_s$ have smaller values at $q^2 = 0$ (but only by $\sim 20\%$) and rise much more steeply with q^2 than is the case with lighter spectator quarks. This trend is exactly the same, but magnified by the larger quark mass change, as that seen for the $b \rightarrow s$ case as we change from a light to a charm spectator (compare Fig. 16).

V. CONCLUSIONS

We have performed the first $N_f = 2 + 1 + 1$ lattice QCD calculation of the scalar, vector and tensor form factors for semileptonic $B \rightarrow K$ decay. As well as including charm quarks in the sea and physical u/d quarks, our calculation improves on earlier work in several ways. We use the relativistic HISQ action for all valence quarks (as well as the sea quarks), extending further the use of HPQCD's heavy-HISQ technique. In contrast to earlier approaches, this method allows us to normalize the weak currents accurately. The scalar and vector currents are completely nonperturbatively normalized here, and the

tensor current uses an α_s^3 -accurate matching from the lattice to $\overline{\text{MS}}$ via a symmetric momentum-subtraction scheme in which nonperturbative artefacts are fitted and removed [42]. The heavy-HISQ approach combines results from multiple heavy-quark masses with multiple values of the lattice spacing and multiple momenta for the daughter meson. The range of possible (physical) heavy-meson masses grows on finer lattices as does the range of daughter-meson momentum. Because the daughter-meson momentum needed to reach $q^2 = 0$ is linear in the heavy-meson mass, this means that we can cover the full q^2 range from q_{max}^2 down to $q^2 = 0$ in our lattice QCD calculation. This is also in contrast to earlier approaches that were restricted to a q^2 region close to q_{max}^2 . Our form factors can be reconstructed using the results in Table V, or by using the code provided, and referring to Appendix A.

Our form factors are compared at the extremes of q^2 to earlier values in Fig. 13. This shows that our uncertainties are a factor of 3 smaller at $q^2 = 0$, and comparable to previous results at q_{max}^2 . For $B \rightarrow K$, our uncertainties on f_0 and f_+ are now below 4% across the whole physical q^2 range and for f_T the uncertainty is below 7% across the same range (see Fig. 10). Our calculational strategy is optimized for $q^2 = 0$ by the use of the temporal vector current. Results using the spatial vector current are more accurate at large q^2 (because of kinematic factors) and we show that in Fig. 5. Uncertainties at large q^2 in our results could straightforwardly be reduced by calculating more correlation functions with the spatial vector current. The important kinematic region for phenomenology is that of small q^2 , however, so we have concentrated on that here. Our statistical uncertainties are dominated by our two finest (and most computationally costly) ensembles (see Fig. 11), and we have demonstrated that our overall uncertainties are dominated by these statistics. They could then be straightforwardly reduced with more computing resources in the future.

Because the heavy-HISQ approach requires multiple values of the heavy-quark mass, a map of the form factors as a function of heavy-meson mass is obtained, connecting those for D to those for B . The form factors are smooth functions of heavy-meson mass in QCD and this is illustrated most clearly by Fig. 13. We can also test expectations from HQET (see Figs. 14 and 15).

Our results here for the vector and scalar form factors for $D \rightarrow K$ are not independent of, and agree with, those given in a recent HPQCD publication [36] based on $D \rightarrow K$ correlators only. Here we give in addition the tensor form factor. For $f_T(q^2, \mu = 2 \text{ GeV})$ we have an uncertainty below 3% across the full q^2 range, roughly halving the uncertainty given in earlier calculations [72]. Our results for $f_T(q^2, \mu = 2 \text{ GeV})$ for $D \rightarrow K$ are significantly higher than those of [72] at large q^2 values. Our form factors can be reconstructed using the results in Table VIII, or from the code provided (see Appendix A).

The smooth connection between $B \rightarrow K$ and $D \rightarrow K$ form factors obtained in the heavy-HISQ approach is a useful one, because at least the $D \rightarrow K$ vector form factor can be compared to accurate experimental results for the semileptonic $D \rightarrow K$ decay process. In [36] it was shown that the shape of the $D \rightarrow K$ vector form factor obtained from lattice QCD using HISQ agrees well with that inferred from the experimental differential decay rate. Since we do not expect new physics in the tree-level $D \rightarrow K$ decay, this is a stringent test of (lattice) QCD. It also provides a firm basis for the $B \rightarrow K$ form factors that we obtain here as an extension to heavier mass of the $D \rightarrow K$ results.

As well as being a smooth function of heavy- (parent) quark mass, form factors in QCD are also a smooth function of spectator quark mass. With accurate form factors covering the full q^2 range now available for a range of processes using the HISQ formalism for all quarks, we can make comparisons that show the impact of changing the spectator quark mass. The conclusion is that very large changes in mass are needed to achieve sizable effects (see Figs. 16 and 20); very little is seen on substituting a strange quark for a light one. Increasing the spectator quark mass by a larger factor (substituting a charm- or bottom quark for a light one) makes the trend clearer, pushing the form factor downwards at $q^2 = 0$ and compressing the q^2 range. More comparisons of this kind will become possible also for pseudoscalar to vector meson decay channels as further sets of form factors become available from lattice QCD. This will yield a more complete picture of form factor behavior with implications for our understanding of meson internal structure.

In an accompanying paper we will lay out in detail the phenomenological implications of the improved form factors for $B \rightarrow K$ that we have calculated here.

ACKNOWLEDGMENTS

We are grateful to the MILC collaboration for the use of their configurations and their code, which we use to generate quark propagators and construct correlators. We would also like to thank L. Cooper, J. Harrison, D. Hatton, and G.P. Lepage for useful discussions and B. Chakraborty, J. Koponen, and A. T. Lytle for generating propagators/correlators in previous projects that we could make use of here. Computing was done on the Cambridge Service for Data Driven Discovery (CSD3) supercomputer, part of which is operated by the University of Cambridge Research Computing Service on behalf of the UK Science and Technology Facilities Council (STFC) DiRAC HPC Facility. The DiRAC component of CSD3 was funded by BEIS via STFC capital grants and is operated by STFC operations grants. We are grateful to the CSD3 support staff for assistance. Funding for this work came from STFC.

APPENDIX A: RECONSTRUCTING OUR RESULTS

Tables V and VIII should allow the reader to reconstruct our form factors using details given in Sec. IV A and Eq. (25). However, to make this easier, we attach an ancillary PYTHON script and text file [75], which will reproduce our fully correlated $B \rightarrow K$ and $D \rightarrow K$ form factors at any q^2 value chosen. The reader should only need a PYTHON installation with the packages GVAR [54] and NUMPY to run this script.

The PYTHON script *make_BK_DK_ffs.py* loads data and correlations from *BtoKandDtoKformfacs.txt* and contains functions *make_fX_Y(qsq)*, where “X” can be “0,” “p” or “T” f_0 , f_+ and f_T respectively and “Y” values of “B” or “D” give the $B \rightarrow K$ or $D \rightarrow K$ form factors. Running ‘python3 *make_BK_DK_ffs.py*’ with *BtoKandDtoKformfacs.txt* in the same directory (and NUMPY and GVAR installed) should produce as terminal output a number of tests. These give the form factors obtained by evaluating the functions at various q^2 values, and compare them with saved results (which are given in the form “c.f. value”). These numbers should agree, and you may also wish to compare the relevant ones with Table VI as a sanity check. After this, using *make_BK_DK_ffs.py* as a module and calling the functions *make_fX_Y(qsq)* from another PYTHON script will report the form factors for any chosen float or GVAR q^2 value. Our form factors are only valid over the physical q^2 range. Values of q^2 outside of the range will result in a warning but will still work, providing they do not cause z to be imaginary.

APPENDIX B: ADDITIONAL COMMENTS ON FORM FACTOR M_H DEPENDENCE

As well as the heavy-mass dependence shown in Fig. 13, we also provide information on the heavy-mass dependence of our form factors at fixed $q^2 = M_D^2$. This dependence for $B \rightarrow \pi$ form factors, which are related to ours by SU(3) flavor symmetry, is of interest in QCD factorization studies of $B \rightarrow D\pi$ (e.g. [76]), where the heavy-mass dependence of $f^{B \rightarrow \pi}(q^2 = M_D^2)$ is expected to be $f^{B \rightarrow \pi} \propto M_H^{-3/2}$. We are able to test this behavior explicitly by varying M_H to reveal the M_H dependence of $f^{B \rightarrow K}(q^2 = M_D^2)$, relevant for a similar analysis to [76], for the $B \rightarrow KD$ decay.

Figure 21 shows the heavy-mass dependence of the form factors at $q^2 = 0$ and $q^2 = M_D^2$. As above, the scale μ is given by Eq. (27). The lower bound on the mass range accessible to us is set at the point where $q_{\max}^2 = M_D^2$. We see that towards $M_H = M_B$, the heavy-mass dependence of the form factors at the two different q^2 is similar, but that this diverges quite rapidly at lower values of M_H , particularly for the vector and tensor form factors.

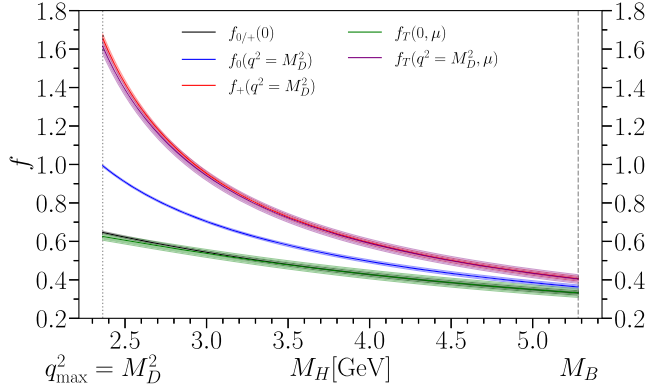


FIG. 21. The M_H dependence of our form factors at $q^2 = 0$ and $q^2 = M_D^2$.

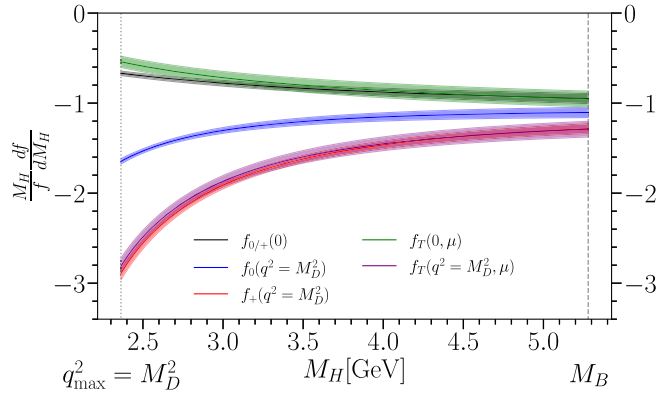


FIG. 22. The dominant power of the M_H dependence of our form factors at $q^2 = 0$ and $q^2 = M_D^2$, isolated using $(M_H/f) \times df/dM_H$.

The dominant power in the M_H dependence is isolated in Fig. 22, by plotting $(M_H/f) \times df/dM_H$ (i.e. returning X if $f \propto M_H^X$). The M_H dependence of the form factors evaluated at $q^2 = 0$ is relatively unchanged (i.e. nearly constant X) for the plotted range of M_H , while the form factors evaluated at $q^2 = M_D^2$ show a more variable exponential dependence.

APPENDIX C: CORRELATOR FIT RESULTS

Table IX gives the results of our correlator fits for the Goldstone kaon, K , for each twist (momentum) on each ensemble listed in Table I. The non-Goldstone kaon (\hat{K}) differs from the Goldstone by discretization effects which we account for in our fit and does not feature directly in our analysis. Likewise, in the last two columns of Table IX we present for each energy the raw fit result E_K^{fit} , as well as the theoretical value, $E_K^{\text{theory}} = \sqrt{M_K^2 + |\vec{p}|^2}$, which again differs only by discretization effects. In practice, we only need to consider E_K in our analysis when we calculate q^2 . In this case, we use the theoretical value as it is more precise, and

TABLE IX. Goldstone kaon energies from fits to correlators on all gluon ensembles. The first column, θ , is the twist value applied, which is converted to $|a\vec{p}|$ (shown in column 2) using $|a\vec{p}_K| = \theta(\sqrt{3}\pi)/N_x$. We then provide the theoretical $E_K^{\text{theory}} = \sqrt{M_K^2 + |\vec{p}|^2}$, which is the value used in our analysis. The fit result, E_K^{fit} , which differs from this only by discretisation effects, is given in the final column.

Set	θ	$ a\vec{p} $	E_K^{theory}	E_K^{fit}
1	0	0.0000	0.37886(17)	0.37886(17)
	2.013	0.3423	0.51059(13)	0.50984(54)
	3.05	0.5186	0.64227(10)	0.6411(17)
	3.969	0.6749	0.773970(85)	0.7702(53)
2	0	0.0000	0.303983(49)	0.303983(49)
	2.405	0.2726	0.408334(36)	0.40820(25)
	3.641	0.4128	0.512611(29)	0.51204(97)
	4.735	0.5368	0.616870(24)	0.6148(23)
3	0	0.0000	0.218672(66)	0.218672(66)
	0.8563	0.0728	0.230473(62)	0.230482(89)
	2.998	0.2549	0.335841(43)	0.33554(88)
	5.140	0.4370	0.488669(29)	0.4884(30)
4	0	0.0000	0.41621(18)	0.41621(18)
	0.3665	0.1246	0.43447(17)	0.43443(19)
	1.097	0.3731	0.55894(13)	0.55735(72)
	1.828	0.6217	0.748141(99)	0.7451(33)
5	0	0.0000	0.33311(11)	0.33311(11)
	0.441	0.1000	0.34780(11)	0.34790(12)
	1.323	0.3000	0.448262(83)	0.44816(35)
	2.205	0.4999	0.600744(62)	0.6001(19)
6	0	0.0000	0.24238(11)	0.24238(11)
	0.4281	0.0728	0.25308(10)	0.25306(12)
	1.282	0.2180	0.325993(79)	0.32565(34)
	2.141	0.3641	0.437369(59)	0.43642(86)
7	0	0.0000	0.160189(88)	0.160189(88)
	1.261	0.1430	0.214698(66)	0.21405(30)
	2.108	0.2390	0.287691(49)	0.28712(73)
	2.946	0.3340	0.370397(38)	0.3693(14)
8	0	0.0000	0.440952(32)	0.4390(25)
	0.706	0.0600	0.118509(63)	0.118509(63)
	1.529	0.1300	0.132843(57)	0.132953(97)
	2.235	0.1900	0.175909(43)	0.17617(22)
	4.705	0.4000	0.223949(34)	0.22405(39)
			0.417213(18)	0.4177(31)

we account for discretization effects elsewhere in our fit. Tables X, XI, and XII contain numerical results from our two- and three-point correlator fits, across all eight gluon ensembles listed in Table I. For each heavy mass and at each q^2 value, we provide the Goldstone heavy-mass M_H , as well as the matrix elements and the form factor values obtained from these via Eqs. (2), (1), and (3). As before with the kaon above, the non-Goldstone heavy-meson mass does not feature directly in our analysis.

TABLE X. Results from fits to correlators on sets 1, 2, and 3, all of which have approximately physical light quark masses. For each heavy quark mass there are four values for the K momentum, giving four different values for q^2 . For each of these values we give the current matrix elements (the matrix elements for the vector and tensor are given before their respective normalisations Z_V and Z_T have been applied). The final three columns give the values for $f_0(q^2)$, $f_+(q^2)$ (in this case only data from V^0 is available) and $f_T(q^2, \mu = 4.8 \text{ GeV})$, determined using Eqs. (1), (2), and (3). No tensor data was calculated on sets 1 or 2.

Set	$(aq)^2$	$\langle K S H \rangle$	$\langle K V^0 \hat{H} \rangle$	$\langle \hat{K} T^{10} \hat{H} \rangle$	$f_0(q^2)$	$f_+^{V^0}(q^2)$	$f_T(q^2)$
am_h							
aM_H							
1	1.1443(10)	2.524(13)	1.792(16)	...	1.0236(49)
0.8605	0.76263(88)	2.236(12)	1.605(14)	...	0.9066(46)	1.133(29)	...
1.44857(46)	0.38113(75)	2.033(18)	1.480(21)	...	0.8243(72)	0.912(14)	...
	-0.00042(62)	1.861(54)	1.425(59)	...	0.755(22)	0.755(22)	...
2	0.72338(50)	2.1519(74)	1.4643(83)	...	1.0240(31)
0.643	0.48244(44)	1.9015(60)	1.3104(68)	...	0.9049(26)	1.123(13)	...
1.15450(30)	0.24166(38)	1.713(10)	1.193(11)	...	0.8154(49)	0.9029(90)	...
	0.00092(32)	1.561(21)	1.093(22)	...	0.7428(98)	0.7430(98)	...
3	0.37848(37)	1.6554(59)	1.0665(83)	...	1.0149(33)
0.433	0.35880(36)	1.6209(59)	1.0463(81)	0.0796(30)	0.9937(34)	1.39(32)	1.199(46)
0.83388(30)	0.18307(30)	1.371(12)	0.900(15)	0.1959(72)	0.8405(71)	0.978(31)	0.843(31)
	-0.07181(21)	1.128(34)	0.776(42)	0.238(17)	0.692(21)	0.661(19)	0.597(42)
3	0.80193(77)	1.8293(87)	1.307(13)	...	0.9916(43)
0.683	0.77563(76)	1.7896(85)	1.279(13)	0.1051(46)	0.9701(43)	1.67(72)	1.501(66)
1.11418(43)	0.54084(67)	1.504(14)	1.080(19)	0.2522(99)	0.8155(78)	1.154(85)	1.028(41)
	0.20028(54)	1.242(41)	0.930(54)	0.300(22)	0.673(22)	0.738(43)	0.714(52)
3	1.03474(98)	1.905(10)	1.407(16)	...	0.9837(49)
0.8	1.00557(97)	1.863(10)	1.376(15)	0.1164(55)	0.9620(48)	1.82(97)	1.634(77)
1.23589(48)	0.74512(87)	1.562(16)	1.154(22)	0.276(11)	0.8067(81)	1.25(12)	1.109(46)
	0.36736(72)	1.293(44)	1.002(59)	0.330(25)	0.667(23)	0.771(65)	0.773(58)

TABLE XI. Results from fits to correlators on sets 4, 5 and 6, all of which have $m_l = m_s/5$. For each heavy quark mass there are several values for the K momentum, giving different values for q^2 . For each of these values we give the current matrix elements (the matrix elements for the vector and tensor are given before their respective normalisations Z_V and Z_T have been applied). The final three columns give the values for $f_0(q^2)$, $f_+(q^2)$ (in this case only data from V^0 is available) and $f_T(q^2, \mu = 4.8 \text{ GeV})$ determined using Eqs. (1), (2), and (3).

Set	$(aq)^2$	$\langle K S H\rangle$	$\langle K V^0 \hat{H}\rangle$	$\langle \hat{K} T^{10} \hat{H}\rangle$	$f_0(q^2)$	$f_+^{V^0}(q^2)$	$f_T(q^2)$
4	1.16024(75)	2.5539(63)	1.8680(99)	...	1.0150(22)
0.888	1.10569(74)	2.5089(58)	1.8358(95)	0.1413(37)	0.9972(20)	1.41(12)	1.192(32)
1.49335(38)	0.73394(65)	2.243(10)	1.660(13)	0.3420(75)	0.8913(40)	1.080(20)	0.964(21)
	0.16885(52)	1.969(34)	1.530(39)	0.430(18)	0.782(13)	0.807(16)	0.727(31)
5	0.73640(43)	2.1641(51)	1.5039(56)	...	1.0083(21)
0.664	0.70142(42)	2.1254(49)	1.4775(54)	0.1124(23)	0.9903(20)	1.40(14)	1.214(26)
1.19125(26)	0.46206(37)	1.9046(63)	1.3326(76)	0.2647(47)	0.8874(28)	1.088(18)	0.953(17)
	0.09877(30)	1.673(20)	1.182(24)	0.322(11)	0.7797(94)	0.811(12)	0.694(23)
	-0.10481(25)	1.557(28)	1.107(33)	0.327(15)	0.725(13)	0.697(12)	0.588(27)
5	1.00245(58)	2.2493(62)	1.6260(68)	...	1.0044(24)
0.8	0.96327(57)	2.2085(59)	1.5966(66)	0.1249(27)	0.9862(23)	1.51(20)	1.316(29)
1.33434(30)	0.69516(51)	1.9761(71)	1.4356(87)	0.2925(55)	0.8824(31)	1.155(27)	1.028(20)
	0.28823(43)	1.733(22)	1.269(26)	0.354(12)	0.7738(99)	0.856(19)	0.747(25)
	0.06019(38)	1.610(31)	1.187(36)	0.361(17)	0.719(14)	0.733(15)	0.635(30)
5	1.21276(70)	2.3094(69)	1.7106(79)	...	1.0031(27)
0.9	1.17065(69)	2.2672(66)	1.6791(76)	0.1335(30)	0.9848(26)	1.59(24)	1.388(32)
1.43437(33)	0.88243(62)	2.0265(77)	1.5073(96)	0.3118(60)	0.8803(32)	1.205(35)	1.081(21)
	0.44500(53)	1.771(23)	1.329(28)	0.376(13)	0.769(10)	0.886(26)	0.782(27)
	0.19987(47)	1.647(33)	1.242(39)	0.384(18)	0.715(14)	0.760(21)	0.665(31)
6	0.38668(32)	1.6875(52)	1.1190(74)	...	1.0089(29)
0.449	0.36819(31)	1.6571(51)	1.0994(75)	0.0830(27)	0.9907(28)	1.40(32)	1.268(41)
0.86422(27)	0.24216(27)	1.4757(74)	0.980(13)	0.1958(50)	0.8823(44)	1.096(41)	0.999(26)
	0.04966(22)	1.279(14)	0.872(25)	0.2405(91)	0.7644(84)	0.791(11)	0.735(28)
	-0.05813(19)	1.210(26)	0.864(46)	0.254(14)	0.723(16)	0.701(16)	0.646(36)
6	0.57131(47)	1.7721(64)	1.2348(98)	...	0.9986(33)
0.566	0.54996(46)	1.7395(62)	1.2124(99)	0.0949(34)	0.9802(32)	1.51(54)	1.407(51)
0.99823(32)	0.40439(41)	1.5451(85)	1.077(16)	0.2218(63)	0.8707(47)	1.181(73)	1.098(32)
	0.18203(35)	1.336(16)	0.951(30)	0.270(11)	0.7531(91)	0.840(25)	0.801(33)
	0.05753(31)	1.268(28)	0.928(50)	0.282(16)	0.714(16)	0.735(19)	0.698(40)
6	0.78019(63)	1.8513(75)	1.341(11)	...	0.9888(37)
0.683	0.75611(62)	1.8165(72)	1.315(11)	0.1054(38)	0.9702(35)	1.62(71)	1.529(55)
1.12566(37)	0.59195(57)	1.6103(94)	1.165(17)	0.2453(70)	0.8601(49)	1.26(10)	1.188(34)
	0.34121(49)	1.392(18)	1.026(32)	0.297(12)	0.7434(94)	0.889(41)	0.861(36)
	0.20081(45)	1.322(31)	0.999(54)	0.310(18)	0.706(17)	0.771(34)	0.748(43)
6	1.00992(80)	1.9254(85)	1.385(42)	...	0.9805(40)
0.8	0.98324(79)	1.8886(82)	1.361(40)	0.1186(82)	0.9618(38)	1.5(2.4)	1.69(12)
1.24733(40)	0.80134(73)	1.672(10)	1.211(49)	0.273(14)	0.8515(50)	1.27(35)	1.299(65)
	0.52349(64)	1.444(19)	1.065(76)	0.330(22)	0.7355(96)	0.92(13)	0.941(63)
	0.36793(59)	1.372(33)	0.967(98)	0.337(28)	0.699(17)	0.853(84)	0.800(66)

TABLE XII. Results from fits to correlators on sets 7 and 8, both of which have $m_l = m_s/5$. For each heavy quark mass there are five values for the K momentum, giving five different values for q^2 . For each of these values we give the current matrix elements (the matrix elements for the vector and tensor are given before their respective normalisations Z_V and Z_T have been applied). The final four columns give the values for $f_0(q^2)$, $f_+(q^2)$ (from both V^0 and V^1 where present) and $f_T(q^2, \mu = 4.8 \text{ GeV})$ determined using Eqs. (1), (2), and (3).

Set am_h aM_H	$(aq)^2$	$\langle K S H\rangle$	$\langle K V^0 \hat{H}\rangle$	$\langle \hat{K} V^1 H\rangle$	$\langle \hat{K} T^{10} \hat{H}\rangle$	$f_0(q^2)$	$f_+^{V^0}(q^2)$	$f_+^{V^1}(q^2)$	$f_T(q^2)$
7	0.16548(20)	1.1890(57)	0.7398(68)	1.0073(45)
0.274	0.10367(17)	1.0435(72)	0.6559(85)	...	0.1241(44)	0.8841(60)	1.071(45)	...	0.997(35)
0.56698(25)	0.02090(14)	0.923(20)	0.591(25)	...	0.1502(76)	0.782(17)	0.808(21)	...	0.722(37)
	-0.072889(96)	0.816(34)	0.529(39)	...	0.156(14)	0.691(29)	0.620(28)	...	0.535(49)
	-0.152895(62)	0.741(55)	0.507(60)	...	0.163(23)	0.628(46)	0.523(49)	...	0.455(65)
7	0.38171(46)	1.3252(88)	0.922(10)	0.9753(60)
0.45	0.29690(42)	1.1584(95)	0.810(11)	...	0.1605(59)	0.8525(68)	1.25(12)	...	1.213(45)
0.77802(37)	0.18332(36)	1.021(24)	0.723(29)	...	0.193(10)	0.751(18)	0.923(75)	...	0.871(47)
	0.05462(30)	0.902(43)	0.647(51)	...	0.200(19)	0.664(31)	0.702(43)	...	0.645(62)
	-0.05516(25)	0.823(68)	0.616(76)	...	0.207(30)	0.606(50)	0.579(42)	...	0.545(79)
7	0.61475(71)	1.426(11)	1.051(13)	0.9493(67)
0.6	0.51181(66)	1.243(11)	0.920(13)	0.1917(48)	0.1870(72)	0.8277(74)	1.38(19)	1.381(28)	1.371(53)
0.94425(46)	0.37396(60)	1.092(28)	0.815(33)	0.2278(92)	0.224(12)	0.727(19)	1.02(14)	1.005(26)	0.980(55)
	0.21777(52)	0.965(50)	0.724(58)	...	0.231(23)	0.643(34)	0.770(92)	...	0.724(72)
	0.08453(46)	0.891(81)	0.698(96)	...	0.240(35)	0.593(54)	0.627(74)	...	0.613(90)
7	0.9854(11)	1.544(14)	1.199(16)	0.9199(77)
0.8	0.8597(10)	1.344(14)	1.046(15)	0.2224(62)	0.2177(83)	0.8009(79)	1.55(30)	1.562(38)	1.554(59)
1.15285(54)	0.69140(93)	1.179(32)	0.917(35)	0.263(11)	0.260(14)	0.703(19)	1.16(22)	1.126(34)	1.109(61)
	0.50070(84)	1.040(57)	0.798(64)	...	0.264(26)	0.620(34)	0.89(17)	...	0.806(80)
	0.33802(77)	0.969(94)	0.78(11)	...	0.275(39)	0.578(56)	0.70(15)	...	0.682(98)
8	0.09183(13)	0.9331(48)	0.5553(58)	1.0120(48)
0.194	0.07974(13)	0.8903(44)	0.5328(57)	...	0.0616(22)	0.9657(45)	1.25(11)	...	1.192(43)
0.42154(22)	0.04344(11)	0.7833(71)	0.4727(91)	...	0.0995(39)	0.8496(77)	0.979(29)	...	0.890(35)
	0.002933(86)	0.699(18)	0.435(22)	...	0.1109(55)	0.758(19)	0.764(20)	...	0.678(34)
	-0.1600035(19)	0.53(11)	0.337(93)	...	0.134(29)	0.58(12)	0.40(11)	...	0.389(84)
8	0.37432(52)	1.137(10)	0.808(10)	0.9491(79)
0.45	0.35338(51)	1.0813(94)	0.7705(94)	0.1036(30)	0.0973(36)	0.9026(72)	1.66(43)	1.743(43)	1.708(64)
0.73033(43)	0.29048(47)	0.943(12)	0.675(13)	0.1660(55)	0.1546(60)	0.7868(97)	1.26(15)	1.295(30)	1.254(49)
	0.22031(43)	0.842(27)	0.620(30)	...	0.1687(86)	0.703(23)	0.92(12)	...	0.936(48)
	-0.06198(27)	0.63(14)	0.46(12)	...	0.182(42)	0.53(11)	0.488(90)	...	0.48(11)
8	0.60243(79)	1.229(14)	0.922(13)	0.9121(95)
0.6	0.57678(78)	1.168(12)	0.877(12)	0.1205(41)	0.1139(45)	0.8667(86)	1.83(70)	1.976(61)	1.949(77)
0.89467(51)	0.49972(73)	1.016(14)	0.766(15)	0.1911(70)	0.1798(72)	0.754(10)	1.40(25)	1.453(42)	1.421(57)
	0.41376(68)	0.911(32)	0.704(35)	...	0.195(10)	0.676(24)	1.00(22)	...	1.056(56)
	0.06795(49)	0.70(17)	0.54(15)	...	0.214(52)	0.52(12)	0.55(16)	...	0.55(13)
8	0.9670(12)	1.341(18)	1.055(17)	0.875(11)
0.8	0.9354(12)	1.273(16)	1.003(16)	0.1411(55)	0.1344(58)	0.831(10)	2.0(1.1)	2.273(86)	2.250(98)
1.10185(60)	0.8405(11)	1.105(18)	0.873(18)	0.2218(91)	0.2114(92)	0.722(11)	1.58(42)	1.657(60)	1.634(71)
	0.7346(11)	0.991(37)	0.799(40)	...	0.228(13)	0.647(24)	1.10(37)	...	1.203(67)
	0.30870(82)	0.65(15)	0.55(15)	...	0.218(53)	0.421(98)	0.50(25)	...	0.55(13)

- [1] N. Cabibbo, Unitary Symmetry and Leptonic Decays, *Phys. Rev. Lett.* **10**, 531 (1963).
- [2] M. Kobayashi and T. Maskawa, CP violation in the renormalizable theory of weak interaction, *Prog. Theor. Phys.* **49**, 652 (1973).
- [3] B. Aubert *et al.* (BABAR Collaboration), Direct CP , Lepton Flavor and Isospin Asymmetries in the Decays $B \rightarrow K^{(*)}\ell^+\ell^-$, *Phys. Rev. Lett.* **102**, 091803 (2009).
- [4] J. P. Lees *et al.* (BABAR Collaboration), Measurement of branching fractions and rate asymmetries in the rare decays $B \rightarrow K^{(*)}l^+l^-$, *Phys. Rev. D* **86**, 032012 (2012).
- [5] J. P. Lees *et al.* (BABAR Collaboration), Search for $B^+ \rightarrow K^+\tau^+\tau^-$ at the BABAR Experiment, *Phys. Rev. Lett.* **118**, 031802 (2017).
- [6] J. T. Wei *et al.* (Belle Collaboration), Measurement of the Differential Branching Fraction and Forward-Backward Asymmetry for $B \rightarrow K^{(*)}\ell^+\ell^-$, *Phys. Rev. Lett.* **103**, 171801 (2009).
- [7] S. Choudhury *et al.* (Belle Collaboration), Test of lepton flavor universality and search for lepton flavor violation in $B \rightarrow K\ell\ell$ decays, *J. High Energy Phys.* **03** (2021) 105.
- [8] T. Aaltonen *et al.* (CDF Collaboration), Observation of the Baryonic Flavor-Changing Neutral Current Decay $\Lambda_b \rightarrow \Lambda\mu^+\mu^-$, *Phys. Rev. Lett.* **107**, 201802 (2011).
- [9] R. Aaij *et al.* (LHCb Collaboration), Measurement of the isospin asymmetry in $B \rightarrow K^{(*)}\mu^+\mu^-$ decays, *J. High Energy Phys.* **07** (2012) 133.
- [10] R. Aaij *et al.* (LHCb Collaboration), Differential branching fraction and angular analysis of the $B^+ \rightarrow K^+\mu^+\mu^-$ decay, *J. High Energy Phys.* **02** (2013) 105.
- [11] R. Aaij *et al.* (LHCb Collaboration), Differential branching fractions and isospin asymmetries of $B \rightarrow K^{(*)}\mu^+\mu^-$ decays, *J. High Energy Phys.* **06** (2014) 133.
- [12] R. Aaij *et al.* (LHCb Collaboration), Angular analysis of charged and neutral $B \rightarrow K\mu^+\mu^-$ decays, *J. High Energy Phys.* **05** (2014) 082.
- [13] R. Aaij *et al.* (LHCb Collaboration), Test of Lepton Universality Using $B^+ \rightarrow K^+\ell^+\ell^-$ Decays, *Phys. Rev. Lett.* **113**, 151601 (2014).
- [14] R. Aaij *et al.* (LHCb Collaboration), Measurement of the phase difference between short- and long-distance amplitudes in the $B^+ \rightarrow K^+\mu^+\mu^-$ decay, *Eur. Phys. J. C* **77**, 161 (2017).
- [15] R. Aaij *et al.* (LHCb Collaboration), Test of lepton universality in beauty-quark decays, *Nat. Phys.* **18**, 277 (2022).
- [16] W. Altmannshofer and D. M. Straub, Cornering new physics in $b \rightarrow s$ transitions, *J. High Energy Phys.* **08** (2012) 121.
- [17] C. Bobeth, G. Hiller, and G. Piranishvili, Angular distributions of $\bar{B} \rightarrow \bar{K}\ell^+\ell^-$ decays, *J. High Energy Phys.* **12** (2007) 040.
- [18] C. Bobeth, G. Hiller, D. van Dyk, and C. Wacker, The decay $B \rightarrow K\ell^+\ell^-$ at low hadronic recoil and model-independent $\Delta B = 1$ constraints, *J. High Energy Phys.* **01** (2012) 107.
- [19] C. Bobeth, G. Hiller, and D. van Dyk, General analysis of $\bar{B} \rightarrow \bar{K}^{(*)}\ell^+\ell^-$ decays at low recoil, *Phys. Rev. D* **87**, 034016 (2013).
- [20] D. Du, A. El-Khadra, S. Gottlieb, A. Kronfeld, J. Laiho, E. Lunghi, R. Van de Water, and R. Zhou, Phenomenology of semileptonic B-meson decays with form factors from lattice QCD, *Phys. Rev. D* **93**, 034005 (2016).
- [21] C. Bouchard, G. P. Lepage, C. Monahan, H. Na, and J. Shigemitsu (HPQCD Collaboration), Standard Model Predictions for $B \rightarrow K\ell^+\ell^-$ with Form Factors from Lattice QCD, *Phys. Rev. Lett.* **111**, 162002 (2013); **112**, 149902(E) (2014).
- [22] A. Khodjamirian, T. Mannel, and Y. M. Wang, $B \rightarrow K\ell^+\ell^-$ decay at large hadronic recoil, *J. High Energy Phys.* **02** (2013) 010.
- [23] W.-F. Wang and Z.-J. Xiao, The semileptonic decays $B/B_s \rightarrow (\pi, K)(\ell^+\ell^-, \ell\nu, \nu\bar{\nu})$ in the perturbative QCD approach beyond the leading-order, *Phys. Rev. D* **86**, 114025 (2012).
- [24] C. W. Bernard, T. Burch, K. Orginos, D. Toussaint, T. A. DeGrand, C. E. Detar, S. Datta, S. A. Gottlieb, U. M. Heller, and R. Sugar, The QCD spectrum with three quark flavors, *Phys. Rev. D* **64**, 054506 (2001).
- [25] C. Bouchard, G. P. Lepage, C. Monahan, H. Na, and J. Shigemitsu (HPQCD Collaboration), Rare decay $B \rightarrow K\ell^+\ell^-$ form factors from lattice QCD, *Phys. Rev. D* **88**, 054509 (2013); **88**, 079901(E) (2013).
- [26] G. Lepage, L. Magnea, C. Nakhleh, U. Magnea, and K. Hornbostel, Improved nonrelativistic QCD for heavy quark physics, *Phys. Rev. D* **46**, 4052 (1992).
- [27] E. Follana, Q. Mason, C. Davies, K. Hornbostel, G. Lepage, J. Shigemitsu, H. Trotter, and K. Wong (HPQCD and UKQCD Collaborations), Highly improved staggered quarks on the lattice, with applications to charm physics, *Phys. Rev. D* **75**, 054502 (2007).
- [28] J. A. Bailey *et al.*, $B \rightarrow Kl^+l^-$ decay form factors from three-flavor lattice QCD, *Phys. Rev. D* **93**, 025026 (2016).
- [29] A. X. El-Khadra, A. S. Kronfeld, and P. B. Mackenzie, Massive fermions in lattice gauge theory, *Phys. Rev. D* **55**, 3933 (1997).
- [30] A. Bazavov *et al.* (MILC Collaboration), Scaling studies of QCD with the dynamical HISQ action, *Phys. Rev. D* **82**, 074501 (2010).
- [31] A. Bazavov *et al.* (MILC Collaboration), Lattice QCD ensembles with four flavors of highly improved staggered quarks, *Phys. Rev. D* **87**, 054505 (2013).
- [32] W. G. Parrott, C. Bouchard, C. T. H. Davies, and D. Hatton (HPQCD Collaboration), Toward accurate form factors for B -to-light meson decay from lattice QCD, *Phys. Rev. D* **103**, 094506 (2021).
- [33] J. Harrison, C. T. Davies, and A. Lytle (HPQCD Collaboration), $B_c \rightarrow J/\psi$ form factors for the full q^2 range from lattice QCD, *Proc. Sci. Beauty2019* (2020) 059.
- [34] L. J. Cooper, C. T. Davies, J. Harrison, J. Komijani, and M. Wingate (HPQCD Collaboration), $B_c \rightarrow B_{s(d)}$ form factors from lattice QCD, *Phys. Rev. D* **102**, 014513 (2020).
- [35] E. McLean, C. Davies, J. Koponen, and A. Lytle (HPQCD Collaboration), $B_s \rightarrow D_s\ell\nu$ Form Factors for the full q^2 range from Lattice QCD with non-perturbatively normalized currents, *Phys. Rev. D* **101**, 074513 (2020).
- [36] B. Chakraborty, W. G. Parrott, C. Bouchard, C. T. H. Davies, J. Koponen, and G. P. Lepage (HPQCD Collaboration), Improved VCS determination using precise lattice QCD form factors for $D \rightarrow K\ell\nu$, *Phys. Rev. D* **104**, 034505 (2021).
- [37] W. G. Parrott, C. Bouchard, and C. T. H. Davies (HPQCD Collaboration), following paper, Standard Model predictions for $B \rightarrow K\ell^+\ell^-$, $B \rightarrow K\ell_1^-\ell_2^+$ and $B \rightarrow K\nu\bar{\nu}$ using

- form factors from $N_f = 2 + 1 + 1$ lattice QCD, *Phys. Rev. D* **107**, 014511 (2023).
- [38] L. J. Cooper, C. T. H. Davies, and M. Wingate (HPQCD Collaboration), Form factors for the processes $B_c^+ \rightarrow D^0 \ell^+ \nu_\ell$ and $B_c^+ \rightarrow D_s^+ \ell^+ \ell^+ (\nu \bar{\nu})$ from lattice QCD, *Phys. Rev. D* **105**, 014503 (2022).
- [39] H. Na, C. T. H. Davies, E. Follana, G. P. Lepage, and J. Shigemitsu (HPQCD Collaboration), The $D \rightarrow K, \ell \nu$ semileptonic decay scalar form factor and $|V_{cs}|$ from lattice QCD, *Phys. Rev. D* **82**, 114506 (2010).
- [40] D. Hatton, C. T. H. Davies, G. P. Lepage, and A. T. Lytle (HPQCD Collaboration), Renormalizing vector currents in lattice QCD using momentum-subtraction schemes, *Phys. Rev. D* **100**, 114513 (2019).
- [41] J. Koponen, C. T. H. Davies, G. C. Donald, E. Follana, G. P. Lepage, H. Na, and J. Shigemitsu, The shape of the $D \rightarrow K$ semileptonic form factor from full lattice QCD and V_{cs} , [arXiv:1305.1462](https://arxiv.org/abs/1305.1462).
- [42] D. Hatton, C. T. H. Davies, G. P. Lepage, and A. T. Lytle (HPQCD Collaboration), Renormalization of the tensor current in lattice QCD and the J/ψ tensor decay constant, *Phys. Rev. D* **102**, 094509 (2020).
- [43] B. A. Kniehl and O. L. Veretin, Bilinear quark operators in the RI/SMOM scheme at three loops, *Phys. Lett. B* **804**, 135398 (2020).
- [44] B. Chakraborty, C. T. H. Davies, B. Galloway, P. Knecht, J. Koponen, G. C. Donald, R. J. Dowdall, G. P. Lepage, and C. McNeile (HPQCD Collaboration), High-precision quark masses and QCD coupling from $n_f = 4$ lattice QCD, *Phys. Rev. D* **91**, 054508 (2015).
- [45] R. J. Dowdall, C. T. H. Davies, G. P. Lepage, and C. McNeile (HPQCD Collaboration), V_{us} from π and K decay constants in full lattice QCD with physical u, d, s and c quarks, *Phys. Rev. D* **88**, 074504 (2013).
- [46] A. Hart, G. M. von Hippel, and R. R. Horgan (HPQCD Collaboration), Radiative corrections to the lattice gluon action for HISQ improved staggered quarks and the effect of such corrections on the static potential, *Phys. Rev. D* **79**, 074008 (2009).
- [47] S. Borsanyi *et al.*, High-precision scale setting in lattice QCD, *J. High Energy Phys.* **09** (2012) 010.
- [48] D. Hatton, C. T. H. Davies, B. Galloway, J. Koponen, G. P. Lepage, and A. T. Lytle (HPQCD Collaboration), Charmionium properties from lattice QCD + QED: Hyperfine splitting, J/ψ leptonic width, charm quark mass, and a_μ^c , *Phys. Rev. D* **102**, 054511 (2020).
- [49] C. Monahan, J. Shigemitsu, and R. Horgan, Matching lattice and continuum axial-vector and vector currents with non-relativistic QCD and highly improved staggered quarks, *Phys. Rev. D* **87**, 034017 (2013).
- [50] D. Guadagnoli, F. Mescia, and S. Simula, Lattice study of semileptonic form-factors with twisted boundary conditions, *Phys. Rev. D* **73**, 114504 (2006).
- [51] G. P. Lepage, B. Clark, C. T. H. Davies, K. Hornbostel, P. B. Mackenzie, C. Morningstar, and H. Trotter, Constrained curve fitting, *Nucl. Phys. B, Proc. Suppl.* **106**, 12 (2002).
- [52] R. J. Dowdall, C. T. H. Davies, R. R. Horgan, G. P. Lepage, C. J. Monahan, J. Shigemitsu, and M. Wingate (HPQCD Collaboration), Neutral B -meson mixing from full lattice QCD at the physical point, *Phys. Rev. D* **100**, 094508 (2019).
- [53] P. Lepage and C. Gohlke, `gplepage/lqfit`: `lqfit` version 11.5.1 (2020).
- [54] P. Lepage, C. Gohlke, and D. Hackett, `gplepage/gvar`: `gvar` version 11.2 (2020).
- [55] P. Lepage, `gplepage/corrfit`: `corrfit` version 8.0.3 (2019).
- [56] C. Bourrely, I. Caprini, and L. Lellouch, Model-independent description of $B \rightarrow \pi \ell \nu$ decays and a determination of $|V_{ub}|$, *Phys. Rev. D* **79**, 013008 (2009); **82**, 099902(E) (2010).
- [57] P. D. Group, Review of particle physics, *Prog. Theor. Exp. Phys.* **2020**, 083C01 (2020).
- [58] N. Husung, P. Marquard, and R. Sommer, Asymptotic behavior of cutoff effects in Yang–Mills theory and in Wilson’s lattice QCD, *Eur. Phys. J. C* **80**, 200 (2020).
- [59] J. Charles, A. Le Yaouanc, L. Oliver, O. Pene, and J. C. Raynal, Heavy to light form-factors in the heavy mass to large energy limit of QCD, *Phys. Rev. D* **60**, 014001 (1999).
- [60] J. Bijnens and I. Jemos, Vector formfactors in hard pion chiral perturbation theory, *Nucl. Phys.* **B846**, 145 (2011).
- [61] C. M. Bouchard, G. P. Lepage, C. Monahan, H. Na, and J. Shigemitsu, $B_s \rightarrow K \ell \nu$ form factors from lattice QCD, *Phys. Rev. D* **90**, 054506 (2014).
- [62] C. Bernard (MILC Collaboration), Chiral logs in the presence of staggered flavor symmetry breaking, *Phys. Rev. D* **65**, 054031 (2002).
- [63] A. Abada, D. Becirevic, P. Boucaud, G. Herdoiza, J. Leroy, A. Le Yaouanc, and O. Pene, Lattice measurement of the couplings g_∞ and $g(B^* B \pi)$, *J. High Energy Phys.* **02** (2004) 016.
- [64] J. Lees *et al.* (BABAR Collaboration), Measurement of the $D^*(2010)^+$ natural line width and the $D^*(2010)^+ - D^0$ mass difference, *Phys. Rev. D* **88**, 052003 (2013); **88**, 079902(E) (2013).
- [65] J. M. Flynn, P. Fritzsche, T. Kawanai, C. Lehner, B. Samways, C. T. Sachrajda, R. S. Van de Water, and O. Witzel (RBC and UKQCD Collaborations), The $B^* B \pi$ coupling using relativistic heavy quarks, *Phys. Rev. D* **93**, 014510 (2016).
- [66] W. Detmold, C.-J. Lin, and S. Meinel, Axial Couplings and Strong Decay Widths of Heavy Hadrons, *Phys. Rev. Lett.* **108**, 172003 (2012).
- [67] F. Bernardoni, J. Bulava, M. Donnellan, and R. Sommer (ALPHA Collaboration), Precision lattice QCD computation of the $B^* B \pi$ coupling, *Phys. Lett. B* **740**, 278 (2015).
- [68] A. Bazavov *et al.*, B - and D -meson leptonic decay constants from four-flavor lattice QCD, *Phys. Rev. D* **98**, 074512 (2018).
- [69] R. J. Hill, Heavy-to-light meson form-factors at large recoil, *Phys. Rev. D* **73**, 014012 (2006).
- [70] C. Bernard and D. Toussaint (MILC Collaboration), Effects of nonequibrated topological charge distributions on pseudoscalar meson masses and decay constants, *Phys. Rev. D* **97**, 074502 (2018).

- [71] L. Riggio, G. Salerno, and S. Simula, Extraction of $|V_{cd}|$ and $|V_{cs}|$ from experimental decay rates using lattice QCD $D \rightarrow \pi(K)\ell\nu$ form factors, *Eur. Phys. J. C* **78**, 501 (2018).
- [72] V. Lubicz, L. Riggio, G. Salerno, S. Simula, and C. Tarantino (ETM Collaboration), Tensor form factor of $D \rightarrow \pi(K)\ell\nu$ and $D \rightarrow \pi(K)\ell\ell$ decays with $N_f = 2 + 1 + 1$ twisted-mass fermions, *Phys. Rev. D* **98**, 014516 (2018).
- [73] N. Gubernari, A. Kokulu, and D. van Dyk, $B \rightarrow P$ and $B \rightarrow V$ form factors from B -meson light-cone sum rules beyond leading twist, *J. High Energy Phys.* **01** (2019) 150.
- [74] B. Colquhoun, R.J. Dowdall, J. Koponen, C. T. H. Davies, and G.P. Lepage, $B \rightarrow \pi\ell\nu$ at zero recoil from lattice QCD with physical u/d quarks, *Phys. Rev. D* **93**, 034502 (2016).
- [75] See Supplemental Material at <http://link.aps.org/supplemental/10.1103/PhysRevD.107.014510> for the attached code allows the user to reproduce our B to K form factor results, as outlined in the associated paper (“ $B \rightarrow K$ and $D \rightarrow K$ form factors from fully relativistic lattice QCD”—W. G. Parrott, C. Bouchard and C. T. H. Davies). For details on how to use the scripts, see Appendix A of that paper.
- [76] M. Beneke, G. Buchalla, M. Neubert, and C. T. Sachrajda, QCD factorization for exclusive, nonleptonic B meson decays: General arguments and the case of heavy light final states, *Nucl. Phys.* **B591**, 313 (2000).